

Fall 2016

Heat Transfer Analysis of an Oblique Jet Impingement Cooling on CMC Rough Surface

Karthik Krishna
Embry-Riddle Aeronautical University

Follow this and additional works at: <https://commons.erau.edu/edt>



Part of the [Aerodynamics and Fluid Mechanics Commons](#)

Scholarly Commons Citation

Krishna, Karthik, "Heat Transfer Analysis of an Oblique Jet Impingement Cooling on CMC Rough Surface" (2016). *Doctoral Dissertations and Master's Theses*. 303.
<https://commons.erau.edu/edt/303>

This Thesis - Open Access is brought to you for free and open access by Scholarly Commons. It has been accepted for inclusion in Doctoral Dissertations and Master's Theses by an authorized administrator of Scholarly Commons. For more information, please contact commons@erau.edu.

HEAT TRANSFER ANALYSIS OF AN OBLIQUE JET IMPINGEMENT COOLING
ON CMC ROUGH SURFACE

A Thesis

Submitted to the Faculty

of

Embry-Riddle Aeronautical University

by

Karthik Krishna

In Partial Fulfillment of the

Requirements for the Degree

of

Master of Science in Aerospace Engineering

Fall 2016

Embry-Riddle Aeronautical University

Daytona Beach, Florida

HEAT TRANSFER ANALYSIS OF AN OBLIQUE JET IMPINGEMENT COOLING
ON CMC ROUGH SURFACE

by

Karthik Krishna

A Thesis prepared under the direction of the candidate's committee chairman, Dr. Mark Ricklick, Department of Aerospace Engineering, and has been approved by the members of the thesis committee. It was submitted to the School of Graduate Studies and Research and was accepted in partial fulfillment of the requirements for the degree of Master of Science in Aerospace Engineering.

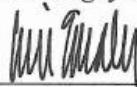
THESIS COMMITTEE



Chairman, Dr. Mark Ricklick



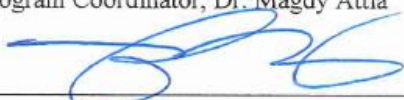
Member, Dr. Magdy Attia



Member, Dr. Luis Gonzalez-Linero



Graduate Program Coordinator, Dr. Magdy Attia



Dean of College of Engineering, Dr. Maj Mirmirani



Vice Chancellor, Academic Support, Dr. Christopher Grant

11.22.2016

Date

11/28/2016

Date

11/22/16

Date

ACKNOWLEDGMENTS

I would like to dedicate this work to my mom Bhagyalakshmi and my dad Krishna who have supported and encouraged me to follow my dreams of becoming an Aerospace Engineer no matter how hard it was for them. A special thanks to my advisor Dr. Mark Ricklick, for his support, patience, guidance, without which this dissertation would not have been possible and for the continuous advice throughout my graduate studies at Embry-Riddle Aeronautical University. I am blessed to have spent time in his tutelage.

I also like to thank all the professors of Department of Aerospace Engineering at ERAU who taught me a tremendous amount of lessons about the academics and about life. I also want to thank Embry-Riddle aeronautical University Research internal grant to fund this study. I would like to thank my lab mates Anish, Christian and Yogesh for helping in my research.

I would like to thank my sister Nandini who always expects great things from me. A special thanks to my best friend Sheetal for all the time she spent critiquing my manuscript and believing in me. Finally, and the most important of everything, I would like to thank my roommates and friends, without your help and encouragement, I could not have achieved this great accomplishment.

TABLE OF CONTENTS

LIST OF TABLES	vi
LIST OF FIGURES	vii
SYMBOLS	ix
ABBREVIATIONS	x
NOMENCLATURE	xi
ABSTRACT	xii
1. Introduction	1
1.1. Thermodynamics	1
1.2. Gas Turbine Cooling	3
1.3. Jet Impingement Cooling	4
1.4. Ceramic Matrix Composite	5
2. Literature Review	6
2.1. Jet Impingement Cooling	6
2.2. Ceramic Matrix Composite	17
2.3. Objective	23
3. Jet Impingement Literature Benchmarking Study	25
3.1. Computational Setup	26
3.1.1. Mesh Independence Study	29
3.1.2. Data Reduction	30
3.2. Results	30
3.2.1. Validation	30
3.2.2. Benchmarking local Nusselt Number	32
3.2.3. Benchmarking local effect of Surface Waviness	34
3.2.4. Benchmarking Average Nusselt Number	35
4. Jet Impingement Experimental Study	37
4.1. Methodology	37
4.2. Experimental Setup	42
4.2.1. Experimental Heat Leakage Test	43
4.2.2. Experimental Data Reduction	46
4.3. Experimental Results	47
4.3.1. Experimental Result Validation	48
4.3.2. Individual Segment Average Results	49
4.3.3. Area-Averaged Nusselt Number	54
5. Experimental Result Benchmarking Study	58
5.1. Computational Setup	58
5.2. CFD Results	59
5.2.1. CFD Results Validation	59

5.2.2.	Benchmarking Area Average Nusselt Number	60
5.2.3.	Benchmarking Individual Segment Average Results	61
6.	Conclusion.....	64
7.	Recommendations	66
	REFERENCES	67

LIST OF TABLES

Table 3.1: Physical properties of the mesh domain	28
Table 5.1: Physical Properties of the mesh domain.....	58

LIST OF FIGURES

Figure 1.1: Brayton Cycle.....	2
Figure 1.2: Evolution of turbine inlet temperature (Ricklick, 2015)	3
Figure 1.3: Jet impingement flow	4
Figure 1.4: CMC coupon (Ricklick, 2015).....	5
Figure 2.1: Reference axis showing the center line	7
Figure 2.2 Centre line Nusselt number (Yan, 1997).....	8
Figure 2.3: Artificially modified rough surfaces (Hansen, 1993).....	10
Figure 2.4: Flow over a 2D wave at $Re = 11,200$ (Wagner, 2010).....	12
Figure 2.5: CMC- I orientation (Top view)	13
Figure 2.6: CMC- II orientation (Top view).....	13
Figure 2.7: Comparison of average Nusselt number (Ricklick, 2015)	14
Figure 2.8: CMC nozzle of GTE (Halbig, 2013).....	19
Figure 2.9: Raw CMC trace (Ricklick, 2015).....	20
Figure 2.10: Filtered profilometer trace containing only waviness (Ricklick, 2015).....	21
Figure 2.11: High resolution local thickness distribution (Ricklick, 2015).....	22
Figure 3.1: Test parameters matching literature experimental setup (Ricklick, 2015).....	25
Figure 3.2: CMC surface dimension matching literature experiments (Ricklick, 2015)..	26
Figure 3.3: Computational domain	27
Figure 3.4: Comparison of local Nusselt number along radial length for $Re= 35,000$	29
Figure 3.5: Comparison of center line Nusselt number plots at $Re = 23,000$	31
Figure 3.6: local Nu for smooth surface jet impingement at $H/D= 6.5$ and $\phi = 45^\circ$	32
Figure 3.7: local Nu for CMC- I surface jet impingement at $H/D= 6.5$ and $\phi = 45^\circ$	33
Figure 3.8: local Nu for CMC- II surface jet impingement at $H/D= 6.5$ and $\phi = 45^\circ$	34
Figure 3.9: Local effect of surface waviness	35
Figure 3.10: Area averaged Nusselt number at $H/D= 6.5$ and $\phi = 45^\circ$	36
Figure 4.1: CNC machined CMC simulated surface	38
Figure 4.2: 3D printed low resolution CMC surface (Ricklick, 2015)	38
Figure 4.3: Schematic of Experimental Set-up.....	40
Figure 4.4: Segmented CMC simulated surface	41
Figure 4.5: Experimental setup.....	43
Figure 4.6: Heat leakage setup (Cross-sectional view).....	44

Figure 4.7: Heat loss versus change in temperature	45
Figure 4.8: Experimental test specimen.....	47
Figure 4.9: Comparison of average Nusselt number against literature.....	48
Figure 4.10: Segmented CMC- I orientation	49
Figure 4.11: Segmented CMC- II orientation	50
Figure 4.12: CMC- N ($\phi = 90^\circ$) impingement case, individual segment average Nusselt number	51
Figure 4.13: CMC- I impingement case, individual segment average Nusselt number ...	52
Figure 4.14: CMC- II impingement case, individual segment average Nusselt number ..	52
Figure 4.15: Comparison of pseudo average Nusselt number at $Re = 35,000$	54
Figure 4.16: Comparison of area averaged Nu for normal ($\phi = 90^\circ$) impingement case..	55
Figure 4.17: Comparison of area averaged Nusselt number at $\phi = 45^\circ$	56
Figure 4.18: Comparison of average Nu for segmented and non-segmented CMC surface at $\phi = 45^\circ$	57
Figure 5.1: Average Nusselt number plot for computational result validation, at $H/D = 7$ and $\phi = 90^\circ$	60
Figure 5.2: Benchmarking area averaged Nusselt number, at $H/D = 7$ and $\phi = 90^\circ$	61
Figure 5.3: Benchmarking segmented averaged Nusselt number for CMC-I case, at $H/D = 7$ and $\phi = 90^\circ$	62
Figure 5.4: Benchmarking segmented averaged Nusselt number for CMC-I case, at $H/D = 7$ and $\phi = 90^\circ$	63

SYMBOLS

A_{cond}	cross-sectional area of conducting plate, m ²
A_{conv}	area subjected to convection, m ²
D	diameter of jet orifice, m
D_h	diameter of heater, m
H	jet to plate distance
h	heat transfer coefficient, Wm ⁻² K ⁻¹
k_{ABS}	thermal conductivity of ABS material, Wm ⁻¹ K ⁻¹
k_{Al}	thermal conductivity of aluminum, Wm ⁻¹ K ⁻¹
k_f	thermal conductivity of fluid, Wm ⁻¹ K ⁻¹
Nu	Nusselt Number
Nu_{avg}	surface average Nusselt number
Nu_{pavg}	segmented local average Nusselt number
Nu_0	surface average Nusselt Number over smooth surface
P	pressure, kgm ⁻¹ s ⁻²
R	radial coordinate of impinging surface, m
Ra	average surface roughness, μm
Re	Reynolds Number
t	thickness, m
T	temperature, K
Wa	average surface waviness amplitude, μm
x	streamwise direction, m
y	spanwise direction, m
z	wall normal direction, m

Greek Symbols

ρ	Density, kgm ⁻³
μ	dynamic viscosity, kgm ⁻¹ s ⁻¹
ϕ	oblique angle of impingement, °

Subscripts

w	refers to wall of simulated surface
j	refers to jet air flow
∞	refers to ambient atmosphere

ABBREVIATIONS

CFD	computational fluid dynamics
CMC	ceramic matrix composite
CPVC	chlorinated polyvinyl chloride
GTE	gas turbine engine
POP	plaster of Paris
sCMC	simulated ceramic matrix composite

NOMENCLATURE

$^{\circ}\text{C}$	Degree Celsius
K	Degree Kelvin
kg/m^3	Kilogram per Meter Cubed
$\text{kg}/\text{m}^*\text{s}$	Kilogram per Meter Second
$\text{kg}/\text{m}^*\text{s}^2$	Kilogram per Meter Second squared
m	Meters
m/s	Meter per Second
$\text{m}^2*\text{K}/\text{W}$	Meters Squared Kelvin per Watt
m^3	Meters Cubed
μm	Micrometer
s	Seconds
W	Watt
$\text{W}/\text{m}*\text{K}$	Watts per Meter Kelvin
W/m^2	Watts per Meter Squared
$\text{W}/\text{m}^2*\text{K}$	Watts per Meters Squared Kelvin

ABSTRACT

Researcher: Karthik Krishna

Title: Jet Impingement Heat Transfer Analysis of a CMC Simulated Surface

Institution: Embry-Riddle Aeronautical University

Degree: Master of Science in Aerospace Engineering

Year: 2016

A Ceramic Matrix Composite is high strength and high temperature capability composite, utilized in components like heat shield of space vehicles, flame holders and disc brakes. To be used in both static and dynamic components of a future gas turbine engine and even with high temperature capabilities of these CMC components, convection cooling will still likely be required. The surface of the CMC varies significantly from traditional super-alloy used in a modern engine, with large level of roughness and significant three-dimensional waviness. These complex features will impact the behavior of the near wall flows, and affect the heat transfer rates both internal and external to the blade. Existing design tools should be updated to account for these effects. As a preliminary investigation into these effects, an obliquely impinging circular jet on a CMC surface is studied. Both experimental and numerical methods are employed to find the effect of simulated surface features on heat transfer rates. In this study, oblique angles of 45° and 90° , jet to plate distance of 6.5 and 7 jet diameters and three Reynolds numbers, 11,000, 23,000 and 35,000, were selected. The test surface is broken down into segments, and individual segment Nusselt numbers are determined and plotted for the various impingement cases studied. Both experimental and CFD results showed negligible changes in average Nusselt number, while local contours were affected. The computational results

were evaluated against literature and experimental results, using v^2f turbulence model. The computational result showed that the local and average Nusselt number for the smooth surface impingement were estimated very close to experimental values and the error was in the range of 14- 17%. In case of impingement over the CMC surface, this model predicted the heat transfer rates close to experimental values in the stagnation region and produced local Nusselt number trends following the experimental results. The impact of the CMC surface feature is negligible compared to the uncertainty in heat transfer coefficient, and therefore traditional design tools can be utilized.

1. Introduction

A gas turbine engine is an efficient and widely used method for power production from chemical fuel. An ever-growing demand for higher power and efficiency, has led researchers to focus their study in this field. A typical gas turbine consists mainly of three main components: compressor, combustor and turbine. A gas turbine compressor, compresses the atmospheric air to high pressure ratio and propels it to the combustor section. The high velocity air is slowed down and energy is added by chemical fuel combustion in this combustor region. The high energy hot gasses are expanded in the turbine and energy is extracted to drive the compressor. The breakthrough research and development in the field of material science and cooling technology has led to the usage of high temperature capable alloys and composites for the hot section of the gas turbine engine (GTE). This has led to a higher turbine inlet temperature and this in turn increased the efficiency and power of the GTE (Boyce, 2011).

1.1. Thermodynamics

A GTE works on an ideal thermodynamic Brayton cycle as shown in Figure 1.1, it shows the importance of cooling with respect to material capabilities. The 1-2 straight vertical line represents the isentropic process of compressing the atmospheric air to high pressure ratio, and increase in temperature from atmospheric inlet temperature (T_1) to the compressed air temperature (T_2). The 2-3 curve represents a constant pressure heat addition process (adiabatic process), increasing the compressed air temperature to turbine inlet temperature (T_3), and this is the maximum temperature attained by the cycle, approximately 1500 Celsius (Halbig, 2013). In the 4-1 isobaric process, energy is extracted and the temperature is decreased from T_4 to T_1 . An equation for gas turbine thermal

efficiency can be derived as a function of state,

$$\eta_{Brayton} = 1 - \frac{T_4 - T_1}{T_3 - T_2}. \quad (1)$$

The atmospheric inlet temperature (T_1) is fixed by ambient condition; the compressed air temperature (T_2) and turbine outlet temperature (T_4) are dependent on the design- pressure ratio. Hence, the only temperature which can be increased is the turbine inlet temperature (T_3). This would cause an increase in cycle efficiency, but it is bounded by the capabilities of materials used. Additional advancement requires cooling of these blades which lead to higher turbine inlet temperature than the safe operating temperature of the material used, thereby increasing the efficiency (Auxier, 2001). Representative temperature limit of a super alloy and a CMC can be seen in the Figure 1.1 (Sommers, 2010).

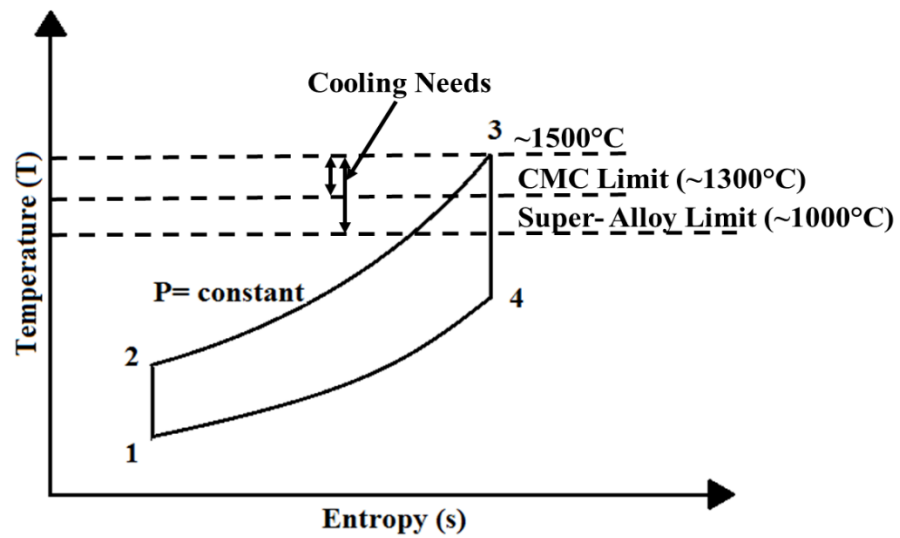


Figure 1.1: Brayton Cycle

1.2. Gas Turbine Cooling

The efficiency and power of a gas turbine engine primarily depends on the turbine inlet temperature and pressure ratio. This temperature is limited by the material capability of the turbine components. Initially in 1950's, increase in turbine efficiency and power was completely dependent on the advancement of material properties. In 1960's and onwards, benefits of cooling technologies were recognized, which had the capability to remove heat from a turbine blade and increase the firing temperature. Various internal and external cooling methods like pin fin cooling, impingement cooling, serpentine cooling, rib cooling and film cooling were employed (Han et al, 2001). Current generation turbine blades are designed in a very complex manner to incorporate both internal and external cooling methodologies. The evolution of the increase in turbine inlet temperature corresponding to the material and cooling methods utilized is shown in Figure. 1.2.

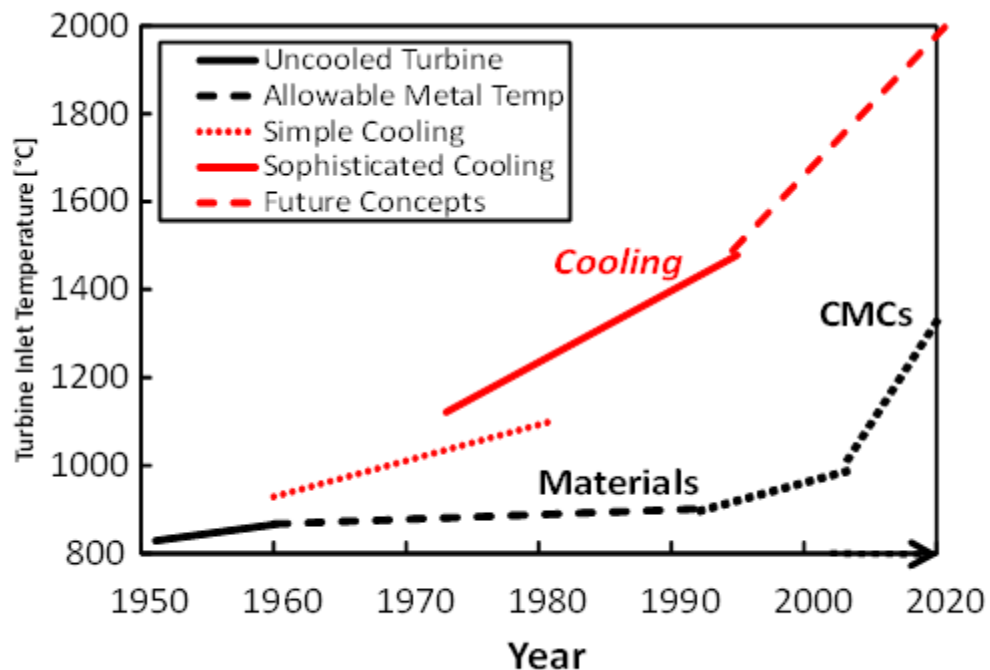


Figure 1.2: Evolution of turbine inlet temperature (Ricklick, 2015)

1.3. Jet Impingement Cooling

Jet impingement cooling is one of the effective internal cooling method utilized in a gas turbine blade. High local and average heat transfer rates associated with jet impingement cooling, has led to its implementation in various other fields like food industry, textile drying and electronic components cooling (Behina et al, 1997).

An impingement flow can be divided into three regions: free jet region, stagnation region and wall jet region, as shown in Fig 1.3. The free jet region is the air jet developed from the nozzle, and the velocity profile of this jet mainly depends on the type of nozzle used. As the jet moves away from the orifice, the jet momentum is lost to overcome the viscous effect of the surrounding free stream region. This effect also causes the jet to extend laterally in length, which can be observed in the Fig 1.3. As the jet approaches the impinging plate, it is deflected into the wall jet region. Here, the axial jet velocity is slowed down as it approaches the plate and converted to radial velocity in the wall jet region. The velocity of the wall jet is higher in the downhill direction than the uphill direction, due to the oblique impingement of the jet. The temperature difference between the impinging flow and hot surface wall, causes heat transfer from the wall surface to the wall jet cooling the surface (Martin, 1977).

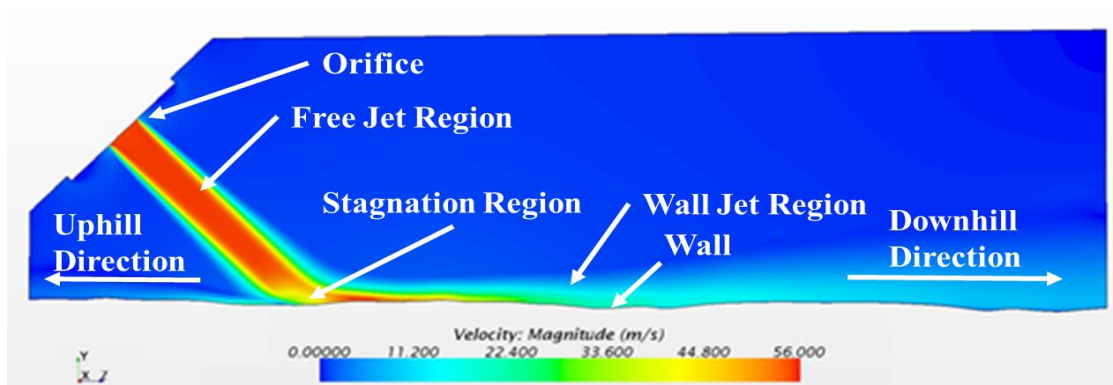


Figure 1.3: Jet impingement flow

1.4. Ceramic Matrix Composite

CMC is a light weight composite material woven using high strength fibers like C/C, SiC/SiC, C/SiC, Alumina etc (Sommers et al, 2010). High mechanical strength and low specific weight of a typical CMC have drawn incredible attention by the gas turbine community for implementation into the core of a GTE (Halbig et al, 2013). A CMC coupon shown in the Fig 1.4, consists of a main-weave thread crossing over another cross-weave thread perpendicularly. The main thread has a lower frequency compared to the cross-weave thread. A thread of a CMC is made up of large number of small fibers therefore this thread is rough in nature. Hence, the surface of this CMC material is an additive of rough and weave surface which varies significantly from a normal rough surface as shown in Fig 1.4 below (Ricklick, 2015).

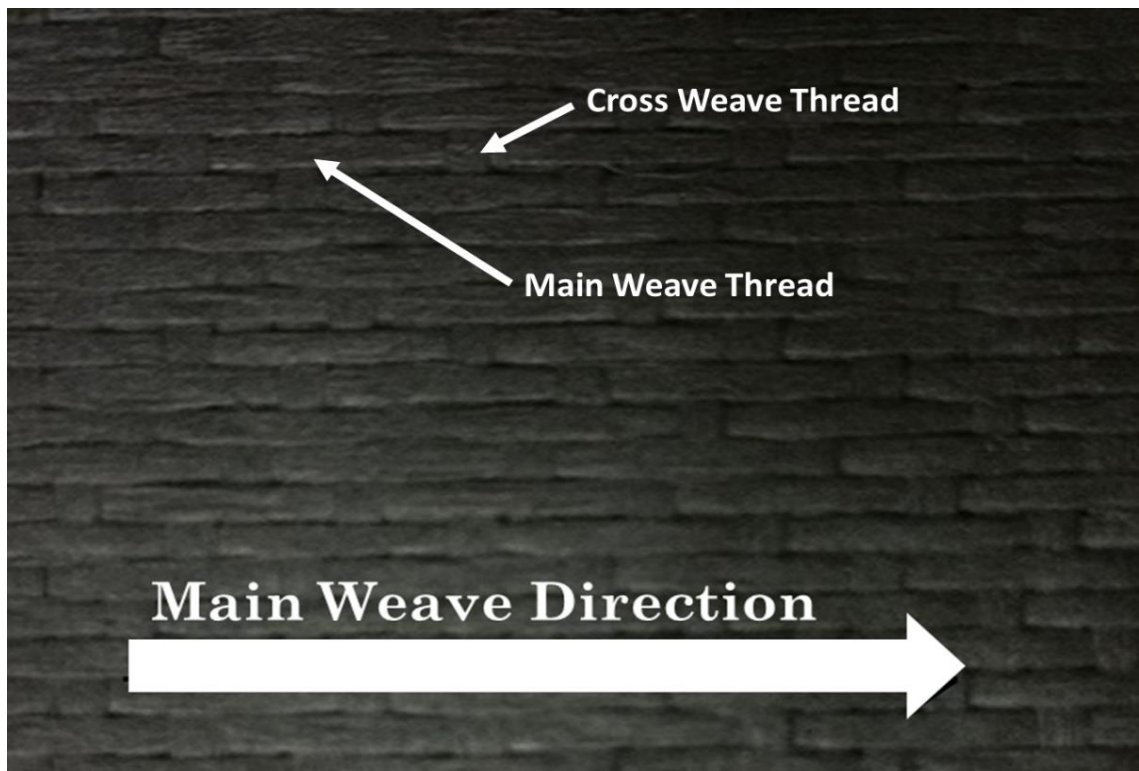


Figure 1.4: CMC coupon (Ricklick, 2015)

2. Literature Review

Gas turbine engines have evolved extensively in last 50 years; efficiency and power are key factors which are improved in this time line. Advancements in the fields of material science, cooling techniques, compressor design and control system have contributed to this improvement. Cooling technique played an important role in increasing power and efficiency to relatively high percentage, due to the proportional effect of turbine blade cooling on the increase in turbine inlet temperature (Koff, 2003).

Jet impingement cooling is an efficient cooling method employed in the regions requiring high local heat transfers rates such as the leading edge of a turbine blade (Downs, 2009). Due to ease of setup and complicated flow features involved in a jet impingement cooling method, this type of cooling is investigated in this study.

2.1. Jet Impingement Cooling

Previous literature works on jet impingement cooling have been summarized and reviewed by Martin (1973). Correlations and results for different impingement parameters like, slot jet, circular jet and row jet impingement have been discussed in detail. Correlations of the average Nusselt number, H/D , Re , D_h and r , for a smooth circular impingement surface are shown in Eqs. 1 and 2. This equation is valid for a Reynolds number of 2,000 to 400,000, r/D_h of 2.5 to 7.5 and H/D of 2 to 12.

$$\frac{Nu_{avg}}{Pr^{0.42}} = \frac{D_h}{r} \frac{1 - 1.1 \frac{D_h}{r}}{1 + 0.1 \left(\frac{H}{D} - 6 \right) \frac{D_h}{r}} F(Re) \quad (1)$$

$$F(Re) = 2Re^{0.5} \left(1 + \frac{Re^{0.55}}{200} \right)^{0.5} \quad (2)$$

Livingood and Hrycak (1973) also summarized the literatures on jet impingement heat transfer. This literature discussed various analytical and experiment approaches for single and row jets. It also summarized and recommended correlations for single and row impingement cooling, for designing turbine blades and other related cooling design needs.

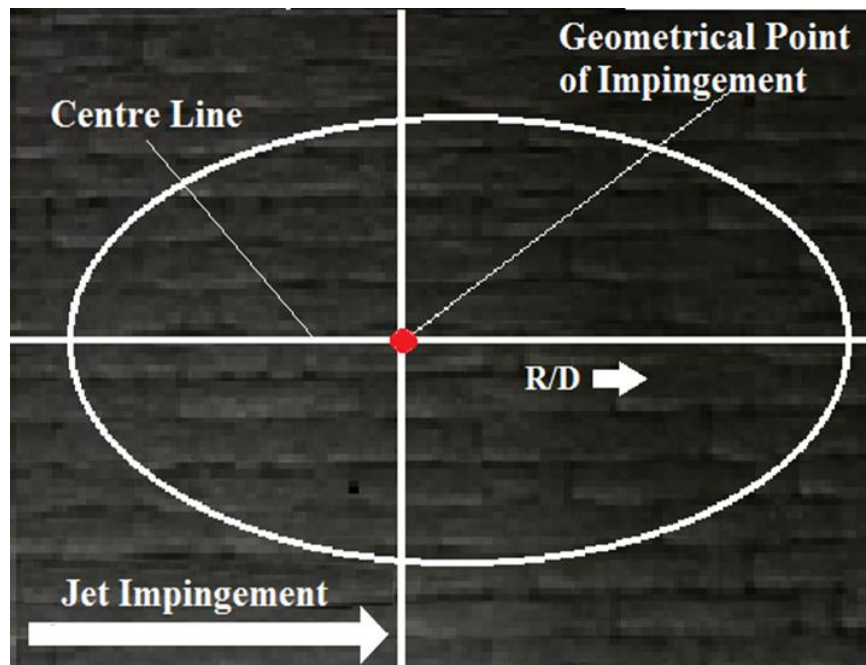


Figure 2.1: Reference axis showing the center line

Yan et al., (1997) investigated the heat transfer characteristics of an obliquely impinging jet on a flat plate, similar to the study carried out in this paper on rough CMC surfaces. They explained that the stagnation point for an obliquely impinging jet moves towards the compression side, yet still lying on the axis of symmetry. The experiment was carried out for various angles of incidence of the impinging jet and corresponding local Nusselt numbers were plotted versus a non-dimensional radial length. The center line along which local Nusselt numbers are determined in this current study is shown in Fig. 2.1. The local Nusselt number plot along this center line for a Reynolds Number of 23,000, H/D of

7 and angle of impingement of 45° is shown in Fig. 2.2. The data plotted is used in this current study for validation of computational results.

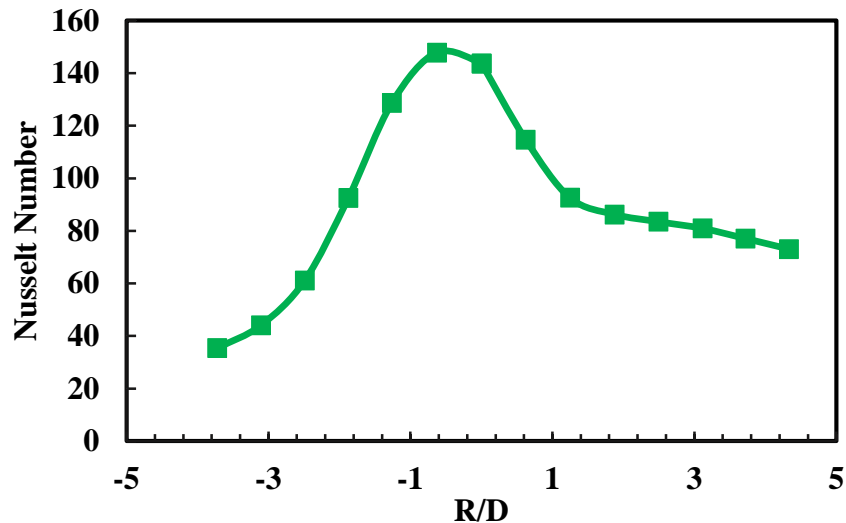


Figure 2.2 Centre line Nusselt number (Yan, 1997)

Similarly, Donovan et al. (2006) experimented at oblique impingement angles of 30° to 90° , for a range of Reynolds numbers from 10,000 to 30,000 and nozzle to plate distance of 0.5 to 8. This study mainly concentrated on the effect of vortices on local heat transfer rates and the region of transition from laminar to turbulent, which is indicated by the secondary peak. This literature also explains the different flow characteristics on uphill and downhill direction of the wall jet.

Jet impingement cooling characteristic on rough surface varies significantly from that of a smooth surface. A collection of literatures are available showing that the jet impingement on the rough surface enhances the heat transfer properties (Chakroun et al. 1998; Nakod et al. 2008; Hansen and Webb, 1993; Beitelmal et al. 2000; Gabour and Lienhard, 1994). In most of these literatures on rough surface, roughness is usually modeled using extended surfaces like pins, ribs, slots and cubes. Chakroun et al. (1998)

experimented on normal jet impingement on a rough and smooth surface to show the effect of roughness. The rough surface used was created by $0.05D$ cubes distributed uniformly on the surface. Results show that, the enhancement in Nusselt number is due to the roughness and the Nusselt number increases with the increase in Reynolds number. The increase in average Nusselt number was in the range of 8.3 to 28% from that of a smooth surface, depending on the Reynolds number and jet to plate distance. Although, the increase in surface area of the rough surface was 7.5% from that of the smooth surface. Similarly, Nakod et al. (2008) performed experiments on finned surface and vortex generators. Experiments were carried out for a Reynolds number range of 7,000 to 30,000 and Z/D of 0.5 to 7. Similar to other literatures, the author concluded heat transfer coefficient was increased for the rough surface. Local results for various fins and vortex generators compared to those of smooth surfaces showed that the vortex generators were more effective than fins.

Kito et al. (2012) studied the effect of ribs placed on a smooth surface on heat transfer rates at a Reynolds number of 5,000. The jet to plate distance was varied from 5 to 20 and the placement of ribs was optimized to enhance the heat transfer rates. It was found that the ribs enhanced the heat transfer rates and for further improvement, the rib spacing should be more than 6 diameters to allow the reattachment of the flow. Gau et al.'s (2000) flow visualization of a circular jet impingement on a triangular rib roughened wall showed that, for a small nozzle to plate distance the cavities formed in the triangular ribs are easier to penetrate than the ones formed in the rectangular ribs. The wide-open cavities allow higher momentum transport between the recirculation flow and the wall jet to easily penetrate these cavities, there by increasing heat transfer. Further, if the nozzle to plate

distance increases, the impinging jet spreads out and transforms into turbulent structures before impinging on to the plate. These coherent structures can easily penetrate the cavities and increase heat transfer rates.

Beitelmal et al. (2000) observed an increase of 6% in average Nusselt number for a rough surface made up of circular protrusions of $0.073D$ base and height. For a circular jet impinging on a rough surface at a Reynolds number of 9,600 to 38,500 and a nozzle exit to plate distance of 1 to 10 jet diameters. Jeevanlal et al. (2014) studied jet impingement heat transfer on indented surface and compared their result against a smooth surface impingement case. The parameters varied are; the jet to plate distance of 1-12 and a Reynolds number range of 10,000- 23,000. Results show that the maximum stagnation Nusselt number was achieved for a Z/D of 6, and a maximum increase in stagnation Nusselt number of 6.78% was observed for a Reynolds number of 60,000.

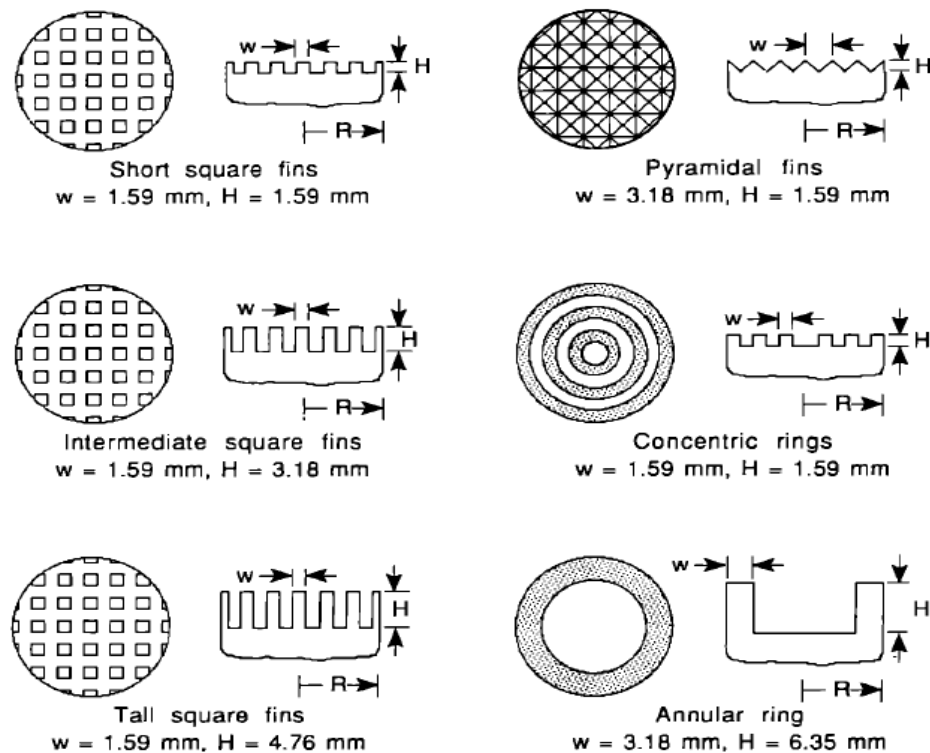


Figure 2.3: Artificially modified rough surfaces (Hansen, 1993)

Hansen and Webb (1993) investigated normal air jet impingement onto a modified surface. The modified surfaces are shown in Fig. 2.3. They classified the modified surfaces based on the area exposed to normal, parallel and oblique surfaces to wall jet. Conclusion stated that the Nusselt number depended on the level of turbulence, velocity of the wall jet and the amount of surface area exposed to parallel, normal or oblique flow. It was also found that the heat transfer was mainly augmented in the order of normal, oblique, and parallel flow. Gabour and Lienhard (1994) investigated jet impingement cooling on rough surfaces with Root Mean Square roughness heights ranging from $0.0005D$ - $0.0064D$, at Reynolds numbers ranging from 20,000-84,000. Results from the experiment showed that the effect of roughness was prominent at higher Reynolds numbers and lower jet diameters. The local Nusselt number at the stagnation point increased with increase in roughness height. Comparing the local Nusselt number with that of a smooth wall showed a 50 percent increase in Nusselt number.

Wagner et al. (2010) performed dynamic large eddy simulations for forced convection heat transfer analysis over 3-dimensional and 2-dimensional wavy surface. The 3D wavy surface is similar to the weave surface of the CMC surface. Results show that vortices are generated for both 3D and 2D wavy surface in the down slope from crest to trough of the wave as shown in Fig. 2.4 and these vortices causes increase in heat transfer rates. It was found that for a Reynolds number of 11,200, a 2D wavy surface was 20% more efficient than a 3D wavy surface. The author also mentioned for a RANS type turbulence model, fine mesh in wall normal direction in the wavy surface is required for predicting accurate result.

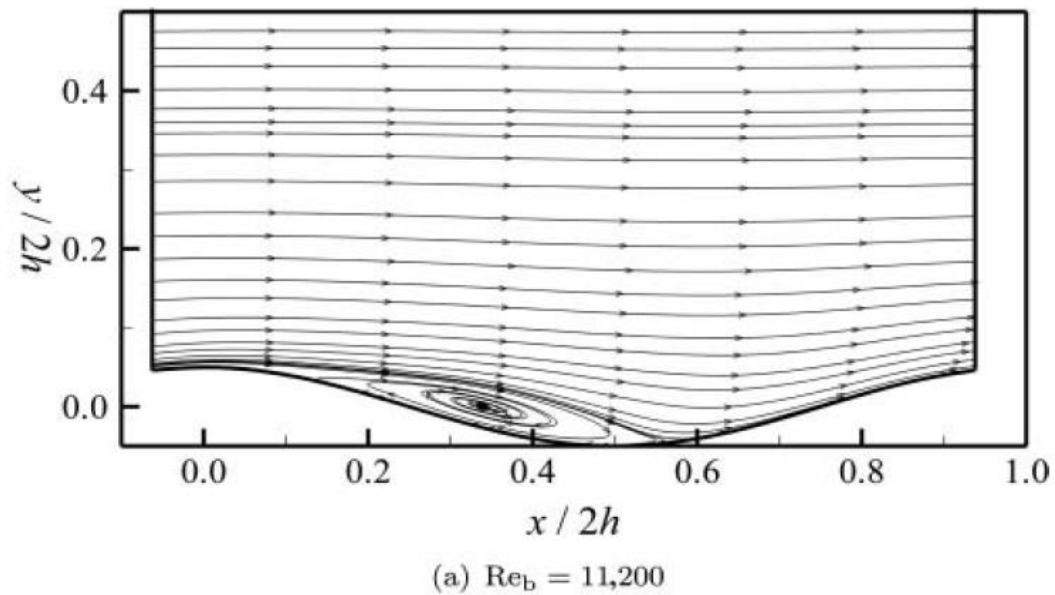


Figure 2.4: Flow over a 2D wave at $Re = 11,200$ (Wagner, 2010)

Preliminary assessment of jet impingement cooling on CMC surface by Ricklick (2015) was carried out on a 3D printed surface, at an oblique angle of 45° and jet to plate distance of 7 jet diameters. The local Nusselt number distribution along the surface was shown in comparison with a smooth surface result. Two types of arrangements were used regarding the CMC simulated surface. Firstly, the air jet aligned parallel to the main weave named “CMC - I”. Secondly, the air jet was kept perpendicular to main weave and named “CMC - II”. These experimental arrangements are shown in Fig. 2.5 and 2.6 respectively; results from these experiments were compared to that of smooth surface impingement results.

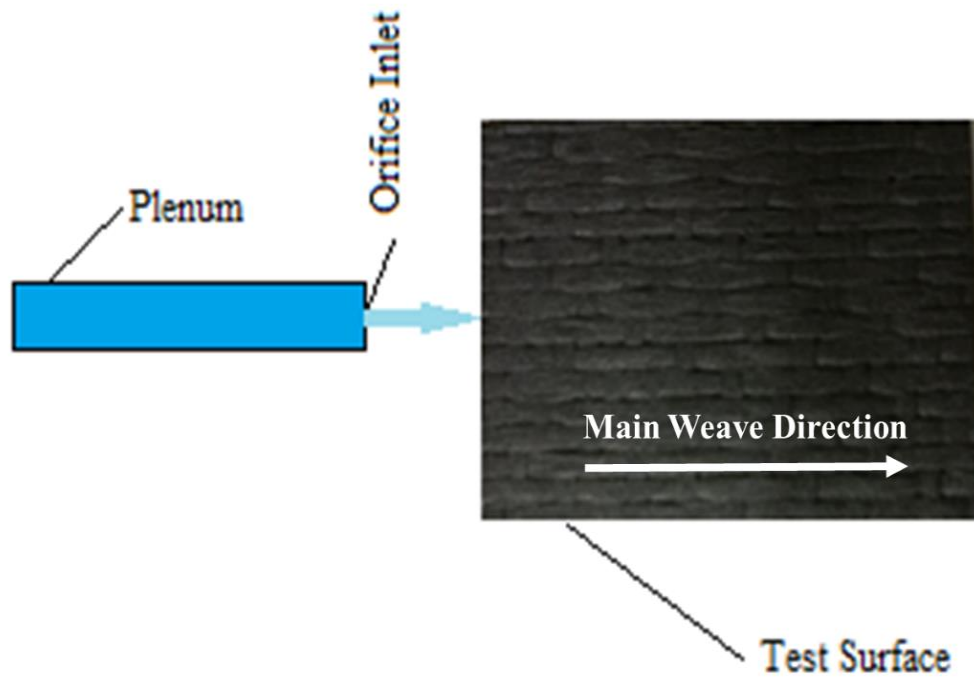


Figure 2.5: CMC- I orientation (Top view)

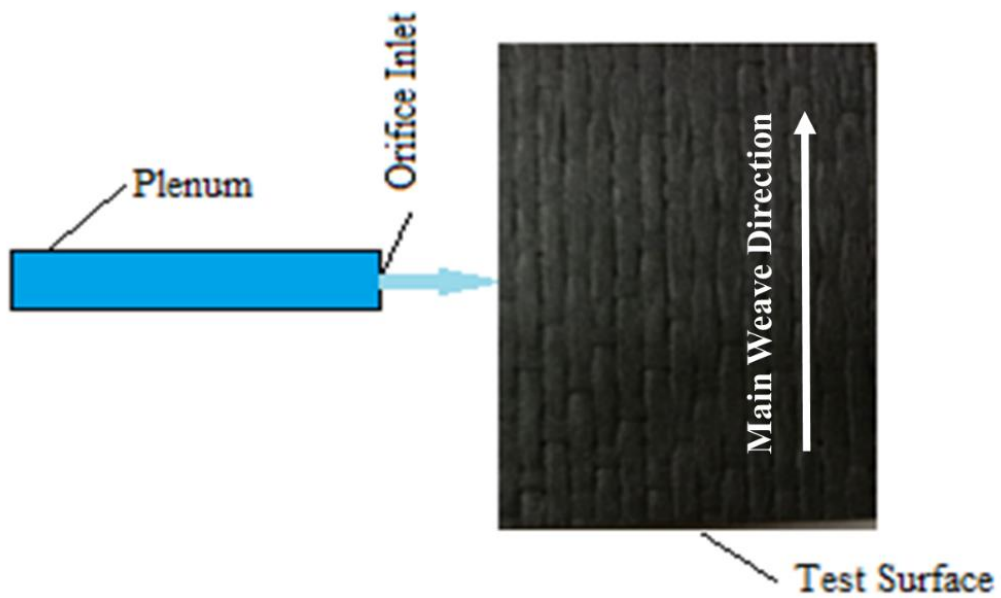


Figure 2.6: CMC- II orientation (Top view)

The average Nusselt number distribution for the CMC surface by comparison with smooth and sand rough surface, at Reynolds 11,000 and 23,000 is shown in Fig. 2.7. The dark line shows the respective area average Nusselt number for the cases tested, and the grey line shows the scaled average Nusselt number compared to the smooth surface impingement case. An augmentation of average Heat Transfer Coefficient (HTC) between 40% and 70% with respect to a smooth surface was observed. The surface profile of the CMC used by the 3D printer, was profiled using a stylus type profilometer from a CMC coupon shown in Fig. 1.4 above and was scaled 6.25X for easiness of printing the surface. The weave feature height varied in the order of 200 to 300 μ m. Due to low resolution of the printer a few features like smoothness of the CMC surface were not recreated from the surface profile data provided. Hence, the increase in heat transfer would be restricted by this factor.

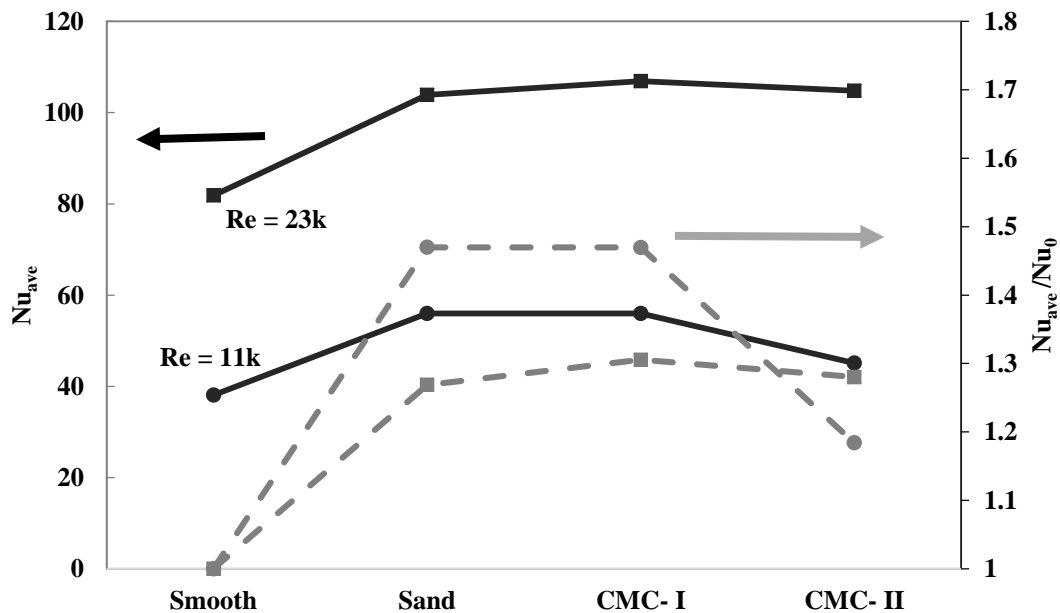


Figure 2.7: Comparison of average Nusselt number (Ricklick, 2015)

The above discussed literatures have shown the augmenting heat transfer effects of rough surfaces under jet impingement cooling, and the rough surface is replicated by artificially modified or protruding small structures. These structures vary significantly from the weave surface. Also, Wagner et al showed the different flow structure for a flow over a wavy surface and its effects on forced convection. Ricklick results showed increase in heat transfer rates locally and in average for jet impingement on CMC surfaces, but the low resolution 3d printed simulated CMC (sCMC) surface also affected this augmentation. Hence, this study intends to further investigate the effect of surface profile with the elimination of the low resolution restricting factor, by using a more accurate manufacturing method to simulate the CMC surface.

Peng et al. (2016) numerically studied jet impingement cooling on 2D modeled wavy rough surface. In this study, the RNG k- ϵ turbulence model was found to be suitable to predict Nusselt number close to the experimental result, and relatively fast when compared with other models. Results showed an overall enhancement of heat transfer rate. A reduction in local Nusselt number at the impingement zone was also observed due to entrapment of fluid in the trough of the wavy wall. Assessment of various turbulence models for a 3 row and 15 columns jet impingement was carried out by Upalkar and Ricklick (2015). The turbulence models investigated were EB- k- ϵ , k- ω (SST), v^2f , realizable k- ϵ , quadratic and cubic k- ϵ . The analysis revealed that the v^2f model results best matched the experimental results followed by EB- k- ϵ for average Nusselt number. Also, the numerical local Nusselt number distribution followed the same trend as that of the experimental result.

Xie et al. (2013) in their numerical study on jet impingement on a dimpled surface, examined various turbulence models like realizable k - ϵ , SST, SST with γ - Re_0 and k - kl - ω models. They used SST with γ - Re_0 for further analysis as it showed good agreement with the experimental results. Numerical analysis was carried out on an obliquely and orthogonally impinging jet, by Alenezi et al. (2015). Four turbulence models were used at a preliminary stage to find the appropriate model for further investigation. For normal impingement, k - ϵ turbulence model showed good agreement with the experimental data out of the other three SST, RSM and SST transport models. In their further analysis using k - ϵ turbulence model, for oblique impingement the model failed to predict the secondary peak. The author concluded that the need for higher level models like LES and DES would be suitable to capture the secondary peak.

Zuckerman and Lior (2005) studied various turbulence models and evaluated these models to predict local Nusselt number for gas jet impingement heat transfer. The turbulence models evaluated were k - ϵ , k - ω , realizable k - ϵ , algebraic stress model, Reynolds stress model, SST, v^2f and DNS/LES unsteady model. The unsteady DNS/LES was found to be the best model to predict the stagnation region Nusselt number and the secondary peak, provided the computational cost was not a factor to be considered, and these models require a very fine mesh and high computational time to solve the Navier-Stokes equation. Considering the computational cost to accuracy ratio, v^2f turbulence model with relatively less computational cost, produced results in the range of 2 to 30% error in Nusselt number prediction and predicted the secondary peak very well. Hence, this paper recommends v^2f model and DNS/LES model for numerical impingement heat transfer studies.

Bovo et al. (2013) analyzed the unsteady characteristics of a single pulse jet impingement on an inclined surface through computational and experimental method. In their computational approach, they have used LES model. Although it was computationally expensive, the model was found to be good enough to predict this type of impingement problems. Behina et al. (1997) studied numerically jet impingement cooling on a smooth surface using v^2f turbulence model. A two-dimensional domain of a grid size of 120×120 was utilized and results showed good agreement with the literature. Additionally, k-epsilon model was also used and results were compared with the v^2f model results. The conclusion stated that the v^2f model predicted local and average Nusselt numbers close to the experimental results. The k-epsilon model over-predicted local values and some results were unrealistic in nature.

From the above review, it can be concluded that DNS/LES, v^2f , EB- k- ϵ and k- ϵ models are more suitable to predict jet impingement heat transfer problems. DNS/LES are the best among the four, but computationally costly. Hence, the second best v^2f model is used in this study for numerical analysis.

2.2. Ceramic Matrix Composite

CMCs have found implementation in various fields like GTE, advanced racing vehicles, aircraft structures and rocket nozzles (Renz et al. 2012; Keller et al. 2011; Orlet et al. 2005). The outstanding mechanical strength, heat resistivity and low thermal conductivity of this composite are the major causes for its exploitation in the specified fields. A CMC is a composite material woven as cloth using high strength fibers like carbon and alumina.

Keller et al. (2011) discussed its implementation as an insulating material for covering the hot section of a GTE. This patent aimed at using the wavy CMC as an insulating surface at a specific amplitude and frequency, to increase the efficiency of the gas turbine engine. This thermal barrier composite in a turbine blade or exhaust duct, is exposed to the high velocity hot gasses. Then the convection heat transfer rate is the preliminary requirement for the design of this insulating material. Keller et al. (2012) in their continuing work, discussed a hybrid structure of wavy CMC surface with internal cooling integrated in it. This invention was to place cooling pipes between two wavy CMC surfaces and to cool the surface internally. Also, this patent proposed that the whole or partial structure should be made up of hybrid CMCs instead of using it as a thermal barrier.

Morrison et al.'s (2004) invention claimed to implement a CMC airfoil with or without an inner core for GTE turbine. Also, it claimed the airfoil could be cooled utilizing advanced internal cooling techniques like jet impingement cooling, cooling passages, trailing edge, and film cooling to increase the turbine inlet temperature. Steibel et al. (2001) proposed the use of ceramic particulate coating on the internal cooling channel surface of the CMC turbine blade, to increase roughness and heat transfer effects locally by varying the particle size. Patents discussed the complicated implementation of CMCs in the GTE. They also urged the need to quantify the effect of CMC surfaces on heat transfer rates.

Sommers et al. (2010) reviewed literatures that discusses various effects and merits of implementing CMC material in a heat exchanger. Additionally, the thermo- mechanical properties, physical/chemical properties and other characteristic were tabulated to assess the implementation of CMCs for heat transfer purposes. Orlet et al. (2005) studied the verification of an effusion cooled CMC rocket thrust chamber, but its performance was not

compared with that of a smooth walled chamber. Bischoff et al. (2012) characterized the structure of a CMC from various samples, and evaluated the influence of surface roughness on non-destructive testing methods. Surface roughness values (Ra) varied along a range of $2.2\mu\text{m}$ to $4.9\mu\text{m}$ depending upon the type of sample.

Halbig et al. (2013) studied and evaluated the impact of application of CMCs for a GTE. A CMC nozzle utilized in this study is shown in Fig. 2.8, the smooth surface finish on the nozzle is due to the application of Environmental Barrier Coating (EBC). The Conclusion stated that a CMC combustor with an EBC can achieve a temperature of almost 1500°C with reduced cooling. Also, this reduction in cooling increased the efficiency and decreased the NO_x emission in the combustion process. They also stressed the lack of literature on heat transfer characterization and cooling design of this material. Zong et al. (2009) experimentation on multi-hole film cooling for a CMC surface also acknowledged the need to study the heat transfer characteristics of a CMC surface.

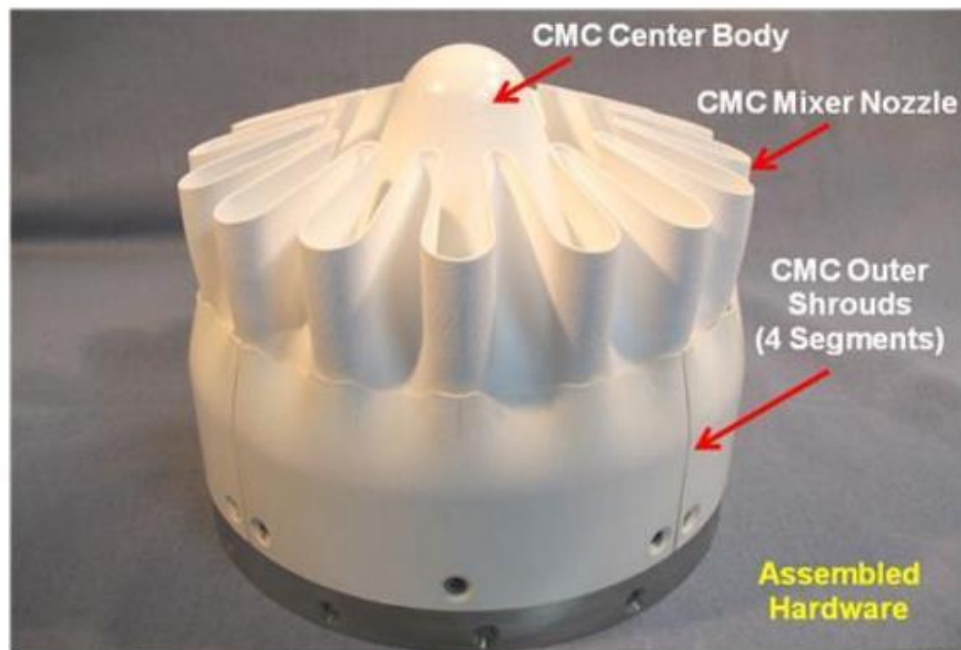


Figure 2.8: CMC nozzle of GTE (Halbig, 2013)

As discussed, Ricklick (2015) performed a preliminary investigation on CMC surface air jet impingement cooling. The literature review showed that there was not sufficient data in the field of surface characterization of a CMC surface. Hence, a CMC surface was characterized for experimentation and simulation of the surface. The full-scale CMC coupon showed in Fig 1.4 was profiled using stylus type profilometer and a manual traverse was used to collect data sets in the third axis at multiple spanwise locations. The two axis profilometer was used to collect data from bottom to top direction, using traverse in the main weave direction, and manual traverse perpendicular to main weave to collect data in spanwise direction. This profiling involved 60 traces along the surface at a resolution of $0.254\mu\text{m}$ and spaced at 0.6mm in the spanwise direction.

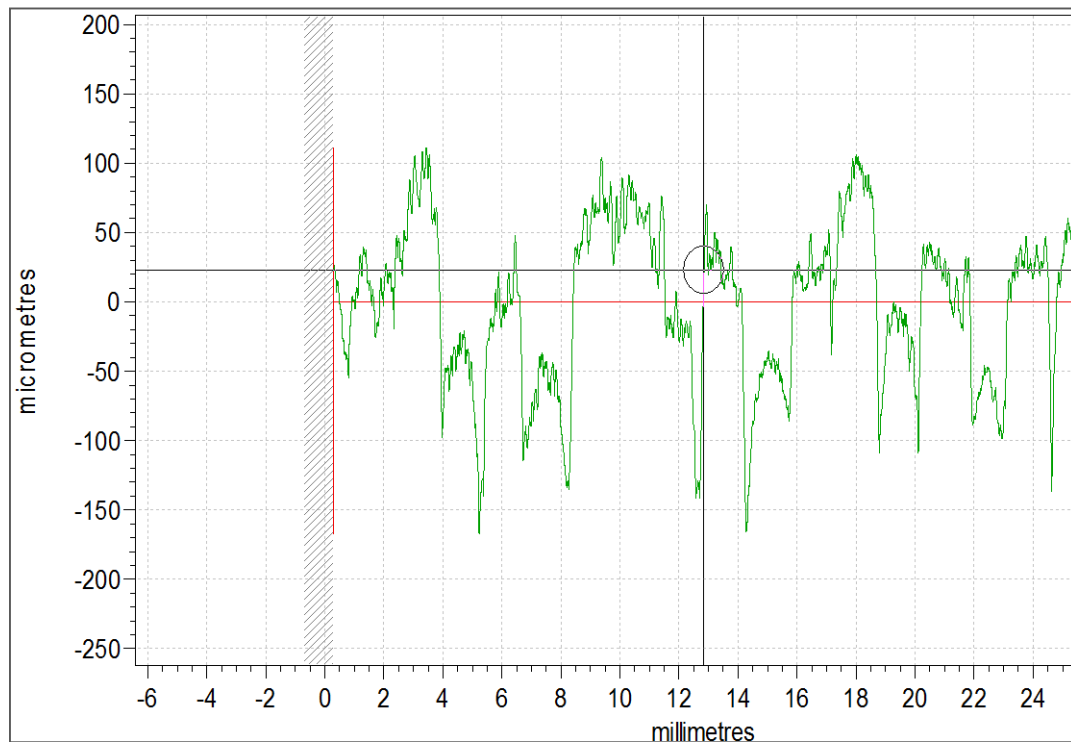


Figure 2.9: Raw CMC trace (Ricklick, 2015)

A typical raw trace of the CMC sample is shown in Fig. 2.9. Here, the X- axis is the direction along the main weave and the Y- axis is the surface height. Primarily, the superimposed wavy and rough features can be observed. The wavy feature can be identified by the large amplitudes and relatively large period. Through analysis of the surface, using Taylor Hobson Ultra software, characteristic roughness (Ra) and waviness (Wa) values were determined. Also by inspection, the maximum change in surface elevation was also determined. The surface roughness (Ra) varied from 5-6 μm , utilizing a low pass filter of 0.25mm. The waviness (Wa) ranged from 35-60 μm , utilizing a low pass filter of 0.8mm. The maximum change in elevation was in the order of 200-300 μm . This data can further be utilized to non-dimensionalize, using the jet diameter.

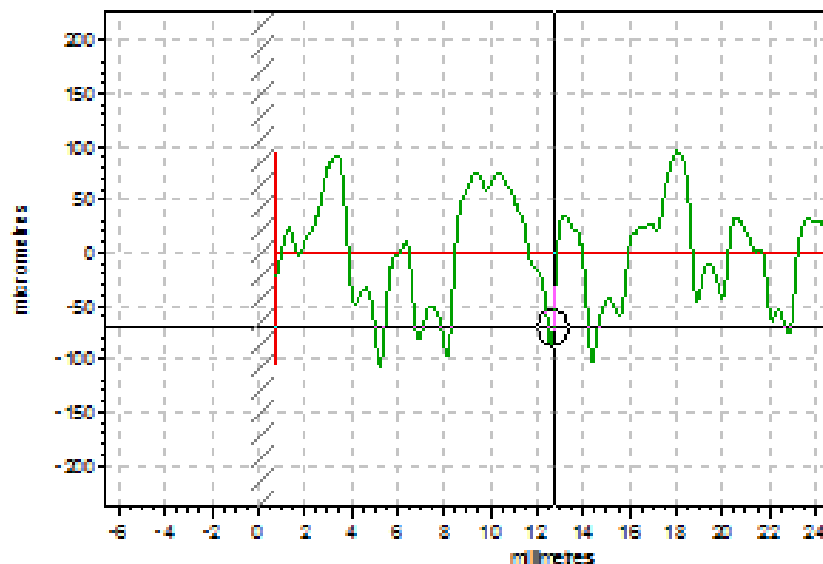


Figure 2.10: Filtered profilometer trace containing only waviness (Ricklick, 2015)

Comparing these values for a super-alloy coated with Thermal Barrier Coating (TBC), typical values would be in the range of 10-14 μm , with a maximum change in

elevation of 96-130 μm . In this work, Boyle (2005) showed that these roughness values affected the heat transfer and laminar to turbulent transition location significantly. Comparing waviness and roughness height, the author concluded that waviness is of concern with the CMC surface. Therefore, the profilometer software was used to filter out the roughness from the trace and project only the waviness, as shown in Fig. 2.10. A MATLAB code was written to parse this cloud of data into a matrix form, such that it could be converted to a CAD usable file. The high resolution local thickness distribution used in this study is shown in the Fig. 2.11.

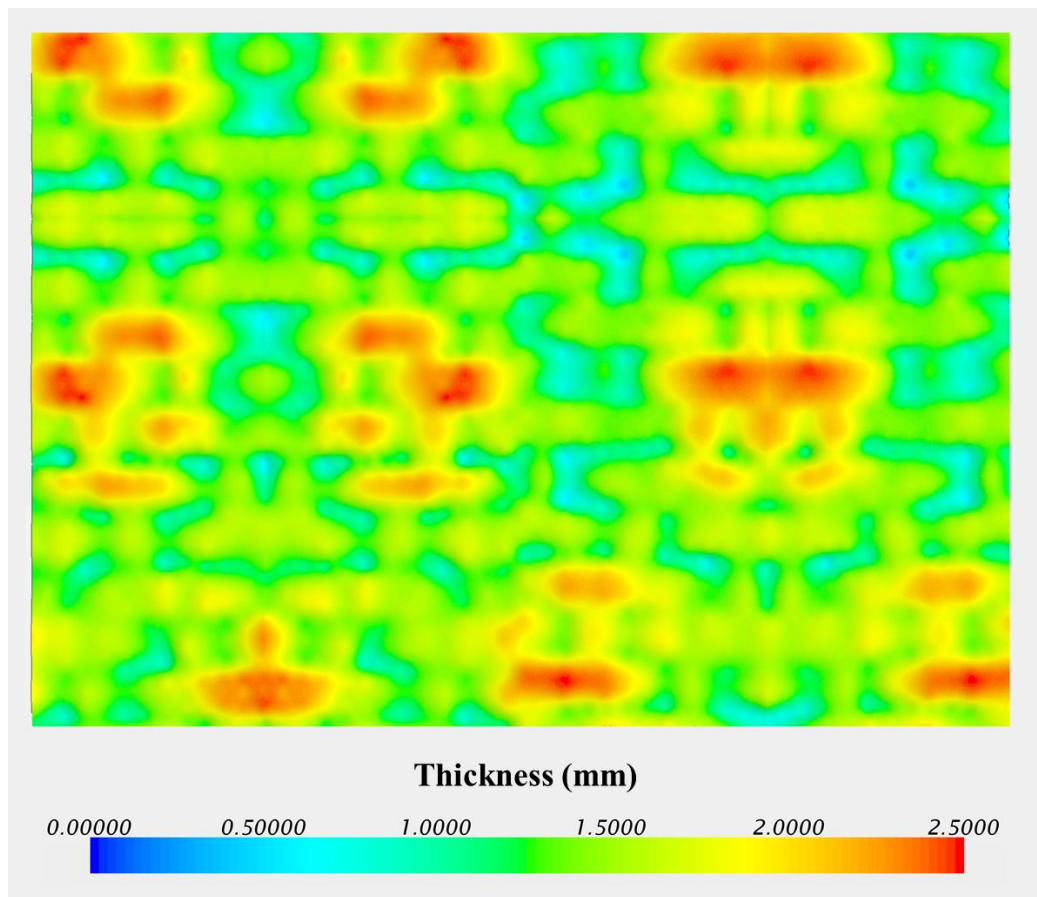


Figure 2.11: High resolution local thickness distribution (Ricklick, 2015)

Available patents and literatures on CMC discuss the implementation of CMC into the core of a GTE with some form of thermal management included and briefly describe the surface texture (Keller, 2011; Keller, 2012; Zong, 2009). Due to insufficient data available in the field of heat transfer rates on CMC- type surfaces, this study aims to determine the heat transfer rates experimentally and computationally, extending the work of Ricklick (2015). The high resolution local thickness distribution captured by Ricklick (2015) is used to investigate experimentally under constant temperature boundary conditions and numerically using commercial CFD software.

2.3. Objective

Existing heat transfer literatures have artificially modeled the surface to illustrate the roughness, whereas the measured CMC surface (Ricklick, 2015) varied from these with a combination of wavy, woven and rough surface texture. The heat transfer on a surface with CMC type features requires examination under typical cooling technique. These impacts should be readily transferable to design tools currently used in industry. The CMC literature reviews discussed the implementation and the surface characteristics briefly. They have also acknowledged the need to study the heat transfer rates of a CMC surface. Ricklick (2015) experimental studies have shown enhancement of local and average heat transfer rates for impingement cooling over a CMC surface. The low-resolution 3D printed surface and methodology used by Ricklick(2015) produced highly uncertain results. Hence, further investigation is required with a reduced uncertainty level.

The objective of this thesis project is to investigate jet impingement heat transfer analysis for a high-resolution CMC simulated surface, experimentally and computationally. This is accomplished by several smaller objectives listed below.

1. The first objective is to computationally benchmark the local and average experimental results of Ricklick (2015) for jet impingement cooling. The tests parameters of this study are jet to plate distance of 6.5 and 7 jet diameters, $\phi = 45^\circ$ and for a Reynolds number of 11,000 and 23,000. The CMC surface simulated is the high-resolution data from the CAD file from Ricklick (2015). Similarly, simulations were carried out on a flat plate to validate the computational results.
2. The second objective is to experimentally investigate the effect of high resolution CMC surfaces on heat transfer rates for impingement cooling. The high-resolution CMC surface CAD file (Ricklick, 2015) was used to machine the smooth weave surface on an aluminum block, in a CNC horizontal milling machine at a spatial resolution greater than was used with the 3D-printed model used by Ricklick (2015) in his experiments. A segmented approach was used to find streamwise average Nusselt number under constant wall temperature boundary conditions. Experiments were carried out for a H/D of 7 jet diameters, impingement angles of 45° and 90° , and for Reynolds numbers 11,000, 23,000 and 35,000. Tests were also carried out on a smooth surface for validation and comparison. The effect of Reynolds number, CMC waviness and angle of impingement on average Nusselt number were determined.
3. The third objective is a computational approach to benchmark the experimental results for all the test cases studied experimentally. Tests were simulated using STAR CCM (version 9.06.009) software and the results were compared against available experimental data.

3. Jet Impingement Literature Benchmarking Study

To understand and evaluate the preliminary effect of the simulated CMC surface on heat transfer coefficient, a benchmarking study was carried out to compare CFD average and local Nusselt numbers against the experimental results of Ricklick (2015). All the experimental cases tested by Ricklick (2015) were modeled and simulated in Star CCM version 9.06.009 software. The experimental test parameters from the literature utilized in this study is shown in the Fig. 3.1.

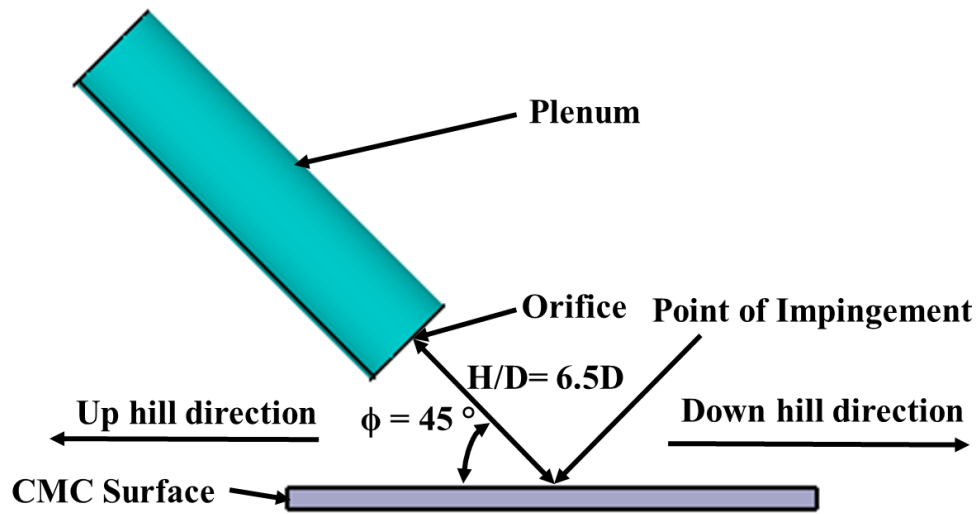


Figure 3.1: Test parameters matching literature experimental setup (Ricklick, 2015)

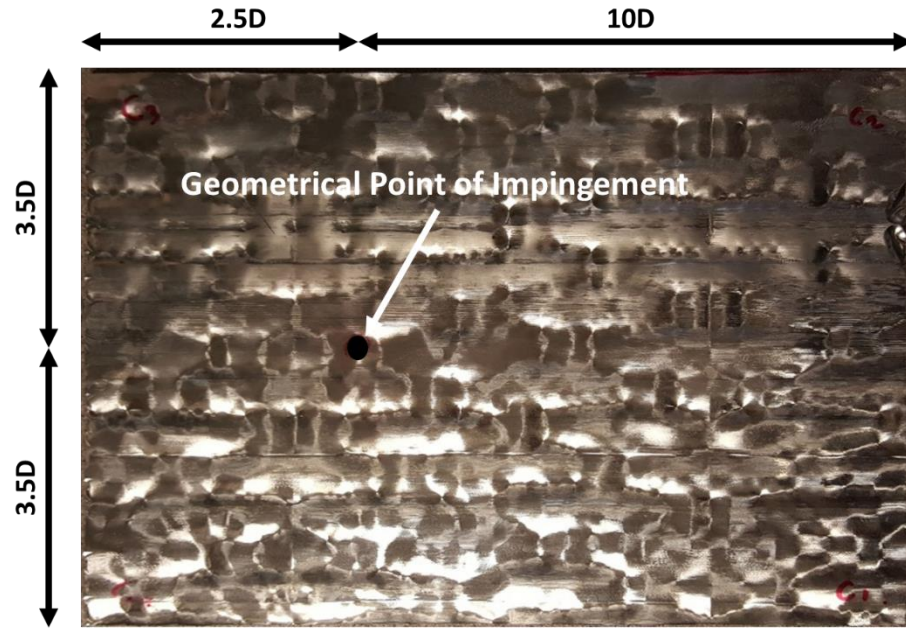


Figure 3.2: CMC surface dimension matching literature experiments (Ricklick, 2015)

The high-resolution CMC surface data imported from the work of Ricklick (2015), simulated in this computational study, is shown in the Fig. 3.2. The dimension of the test surface and the point of impingement are also specified.

3.1. Computational Setup

The computational domain was setup equivalent to the Ricklick (2015) experimental setup shown in Fig. 3.1. Due to the wavy nature of the CMC surface, a three-dimensional conduction analysis should also be carried out along with the Navier-Stokes equation for fluid flow. Hence, a conjugate heat transfer problem was solved.

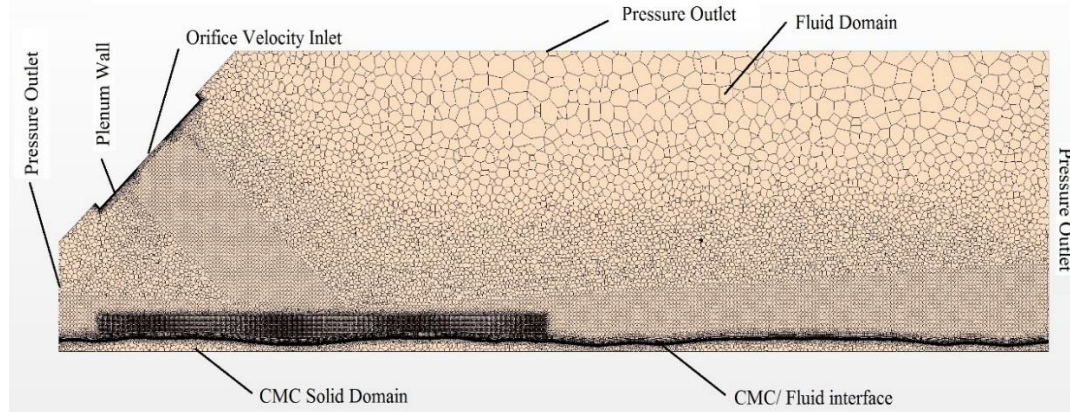


Figure 3.3: Computational domain

The domain was constructed for the whole sCMC surface plate dimension; a rectangular block was extruded from the CMC plate and a plenum with an orifice was placed into position matching the conditions of the literature setup. Later, the rectangular block was cut parallel to the orifice to decrease the mesh size. The conjugate mesh domain is shown in Fig. 3.3. The mesh domain simulating the air was given a pressure outlet condition and the 2D surface featuring the orifice was given a velocity inlet boundary condition.

The turbulence is modeled by v^2f model; this model was selected after a comprehensive literature review (Section 2.1) considering the accuracy to computational cost ratio as an important factor. This is a near wall turbulence model and it does not use a wall function to determine the velocity profile near the wall in the sub-viscous layer (wall $y^+ < 1$), instead local velocity is computed up to the solid wall. Hence, large number of cells are densely modeled near the wall to maintain a wall $y^+ < 1$, which is one of the basic requirements for this type of problem (Wang et al. 2008).

The table featuring all the physical properties used in this approach are shown in Table.3.1. The 3D solid CMC domain was meshed directly on the imported 3D IGES characterized CMC model (Ricklick, 2015). All the faces were set to be an adiabatic wall, and the bottom wall was given a constant temperature for all the trails. A volumetric mesh refinement was used to finely mesh the stagnation and wall jet region, the max cell size in this region was 0.02D. Similarly, the sCMC surface was replaced by a flat plate using the same impingement properties and the flat plate was given a thickness of 2.5mm. This simulation results were used to validate and compare the CFD results with literature of Yan (1997) and Ricklick (2015).

Table 3.1: Physical properties of the mesh domain

Description	Values
Atmospheric temperature (K)	$T_{\infty} = 300$
Atmospheric pressure ($\text{kgm}^{-1}\text{s}^{-2}$)	$P_{\infty} = 101325$
Density of air (kgm^{-3})	$\rho = 1.18415$
Dynamic viscosity of air ($\text{kgm}^{-1}\text{s}^{-1}$)	$\mu = 1.855 \times 10^{-5}$
Jet diameter (m)	$D = 0.006858$
Non-dimensional nozzle to plate distance	$H/D = 6.5 \text{ \& } 7$
Temperature of bottom wall (K)	$T_w = 344.9$
Temperature of impinging jet (K)	$T_j = 300$
Thermal conductivity of fluid air ($\text{Wm}^{-1}\text{K}^{-1}$)	$k_f = 0.0260305$
Thermal conductivity of solid ($\text{Wm}^{-1}\text{K}^{-1}$)	$k_{\text{ABS}} = 0.14$

3.1.1. Mesh Independence Study

Grid independency study was carried out by comparing the change in local temperatures for four points picked randomly near the stagnation region. The mesh independency was carried out for three mesh counts for the CMC surface simulation and two mesh counts for smooth surface simulation, independently for the highest Reynolds number of 35,000. For the CMC- I surface simulation the three-mesh cell count was approximately 21million, 26 million and 40 million. The maximum percentage change in temperature was 0.07%. Hence, the medium mesh count 26million was used for further simulations. For the smooth surface simulation, the two-mesh cell count was approximately 35 million and 46 million. The maximum percentage change in temperature was 0.01%. Hence, the lower mesh count was used for further simulations. The local Nusselt number distributions for the mesh sizes for CMC- I are showed in the Fig. 3.4. The local Nusselt numbers for all the cases are found overlapping each other stating that the results are mesh independent. For further numerical investigation, the CMC 26 million mesh and similarly for the smooth surface, 35 million mesh size were used.

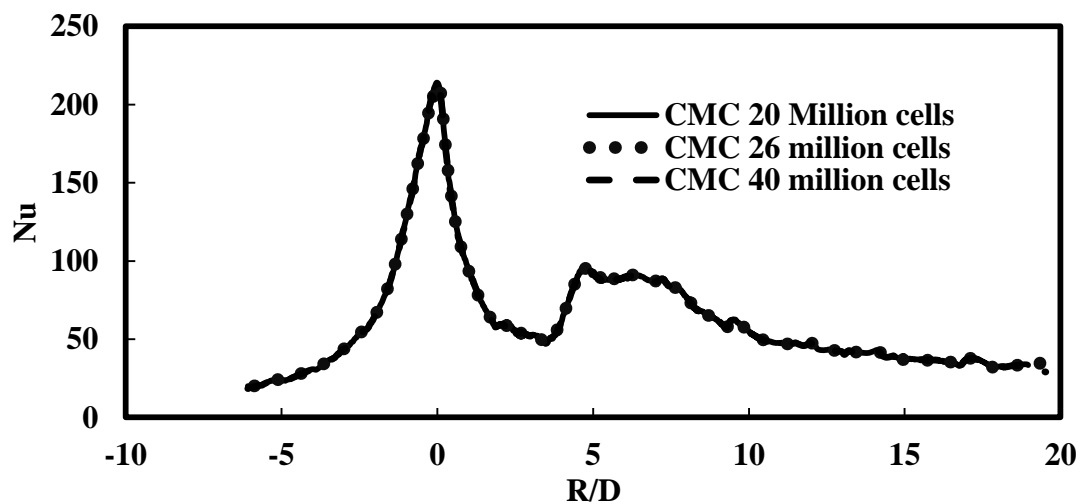


Figure 3.4: Comparison of local Nusselt number along radial length for Re= 35,000

3.1.2. Data Reduction

In this benchmarking study, Reynolds number was established at the orifice of the nozzle with a velocity inlet condition. The Reynolds number tested here are 11,000 and 23,000. The velocity at the orifice was calculated at these Reynolds number using the equation 3, based on the orifice diameter of 6.858mm. The Nusselt number was determined using the equation 4, the characteristic length used is the orifice diameter.

$$Re = \frac{\rho v D}{\mu} \quad (3)$$

$$Nu = \frac{h D}{k_f} \quad (4)$$

3.2. Results

Computational local and area average results are compared with the experimental results of Ricklick (2015). The local result is plotted along the center line on the geometrical point of impingement as shown in Fig. 2.1. These local values are averaged to find average Nusselt number. The area along which the local values are averaged is shown in Fig. 3.2.

3.2.1. Validation

For the validation of computational results, the center line local Nusselt number distribution for the flat plate impingement was compared with the literatures experimental data. The data plotted in Fig. 3.5 shows a comparison for smooth flat plate impingement at a Reynolds number of 23,000 for the Yan (1997) experiment, computational and Ricklick (2015) experiment results. The computational results are closely matching the literature on the uphill side and the local Nusselt number drops as the radial length increases, on the

downhill side. The error in predicting the stagnation Nusselt number by the v^2f model is 3.7% with respect to Ricklick's (2015) experimental result. Further, the computational result for a H/D of 6.5 predict values close to the literature (Yan, 1997) result and the error in predicting the stagnation Nusselt number is 2.96%. It can be concluded that, the v^2f model predicts the stagnation Nusselt number and local Nusselt number on the uphill side accurately but this accuracy decreases with the increase in radial length on the downhill side. The computational results follow the same trends as that of the literature and the error is also acceptable. Therefore, the following computational runs performed are assumed acceptable.

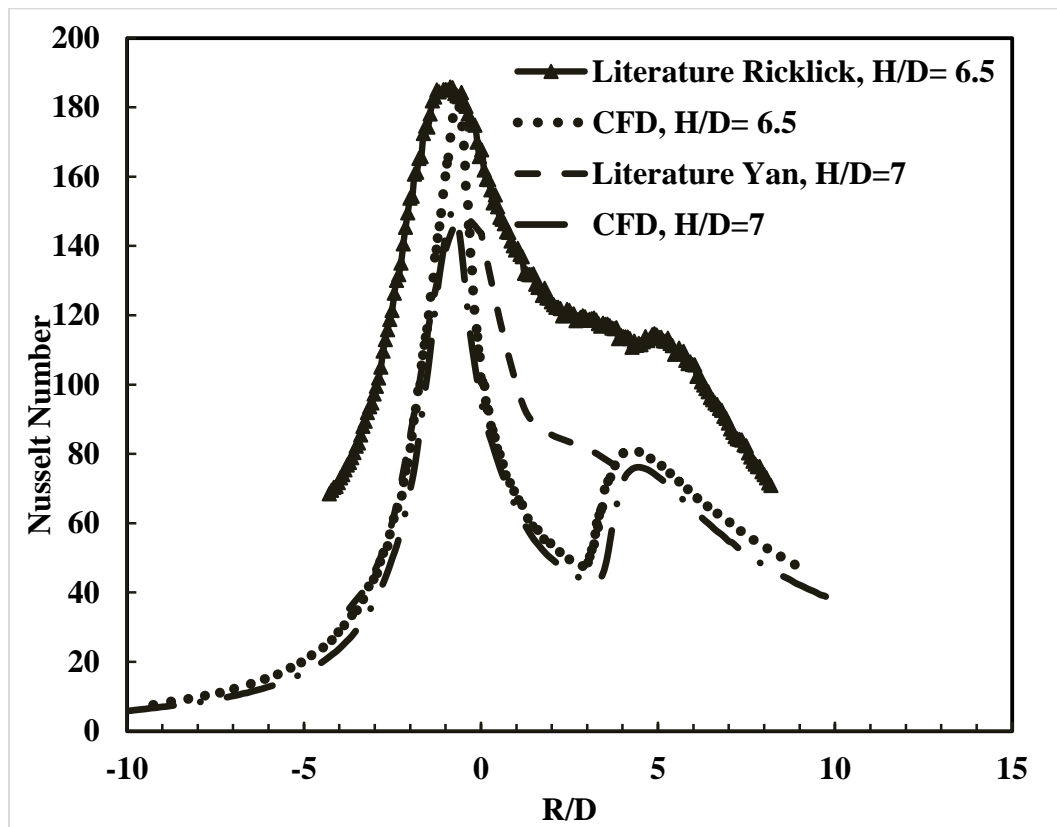


Figure 3.5: Comparison of center line Nusselt number plots at $Re = 23,000$

3.2.2. Benchmarking local Nusselt Number

Computational and experimental (Ricklick, 2015) data representing the local distribution of Nusselt number for smooth surface jet impinging obliquely at 45° and at an H/D of 6.5, is shown in Fig. 3.6. The numerical model predicts the stagnation Nusselt number very close to experimental Nusselt number. The error in predicting the stagnation Nusselt number is 2.96% and 4.15% for Reynolds number of 11,000 and 23,000 respectively. This model tends to produce nearly accurate local results for the lower Reynolds number and error increases for the higher Reynolds number, also the secondary peak in the numerical result is exaggerated compared to the flat or no peak in literature result.

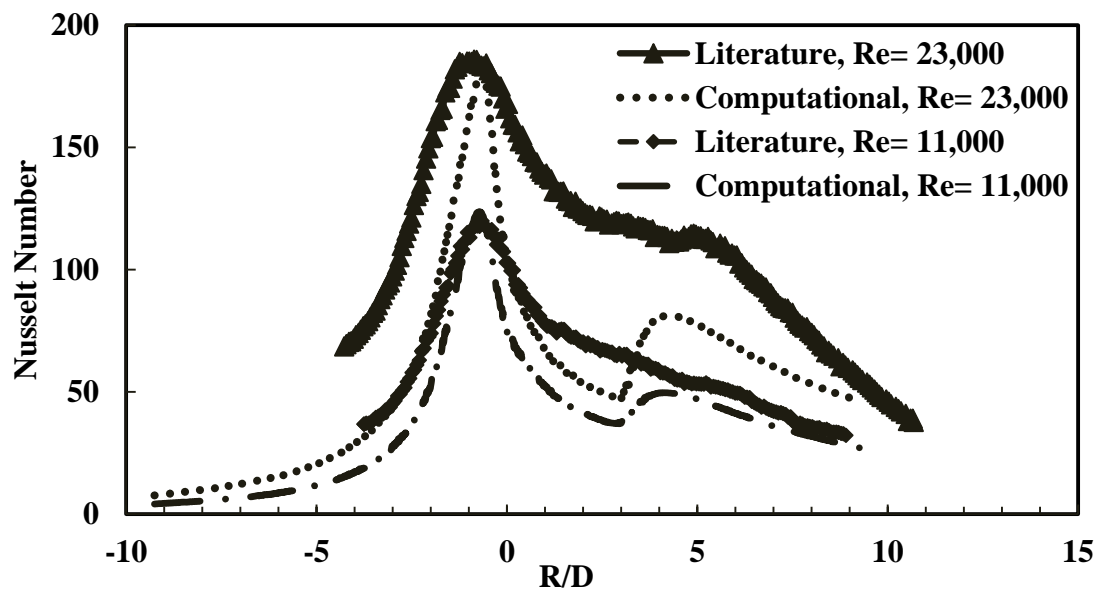


Figure 3.6: local Nu for smooth surface jet impingement at $H/D= 6.5$ and $\phi = 45^\circ$

Comparing the computational and Ricklick experimental results of the local Nusselt number distribution for the jet impingement parallel to the weave at H/D of 6.5 and at oblique impinging angle of 45° are shown in Fig. 3.7. The numerical result follow the same

trend as that of the literature experimental result, the error in predicting the local Nusselt number are higher for the higher Reynolds number. In case of the lower Reynolds number, the local data predicted by the numerical model is very close to the exact value. The numerical model also predicts the position of the secondary peak close the exact location in both the cases.

For the CMC surface jet impingement, perpendicular to the main weave (CMC- II), computational and Ricklick experimental results are shown in Fig. 3.8. It can be observed that, the literature local distribution along the weave surface structure is also replicated by the computational result to some extent, but there is an offset of the secondary peak as observed above for the parallel weave impingement. The v^2f model predicts the stagnation Nusselt number for the low Reynolds number close to the exact value, whereas this error increases for the higher Reynolds number. Although the computational model predicts the secondary peak, it is unable to predict the smaller peaks.

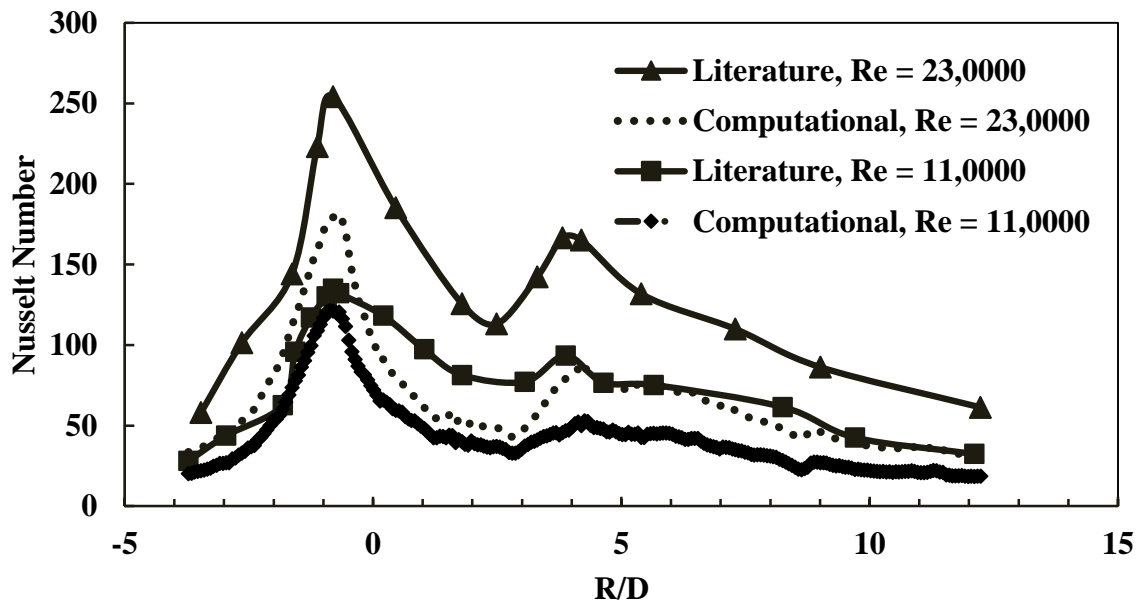


Figure 3.7: local Nu for CMC- I surface jet impingement at $H/D= 6.5$ and $\phi = 45^\circ$

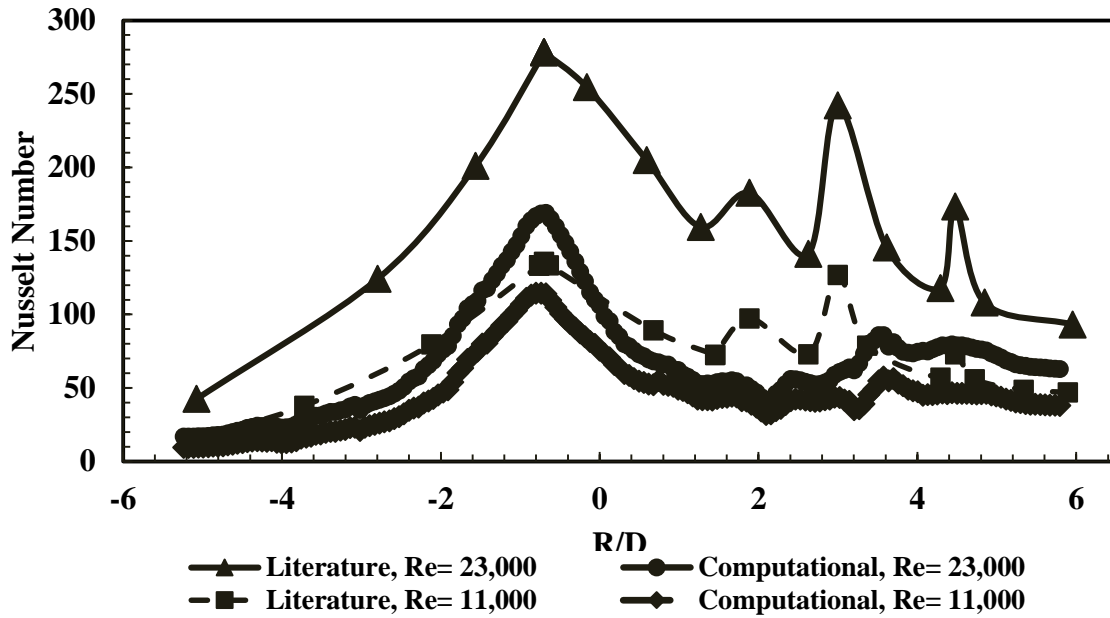


Figure 3.8: local Nu for CMC- II surface jet impingement at $H/D= 6.5$ and $\phi = 45^\circ$

3.2.3. Benchmarking local effect of Surface Waviness

The figure 3.9 shows the high resolution local experimental result (Ricklick, 2015) and computational local Nusselt number distribution for an H/D of 6.5 and Reynolds number of 11,000 along with simulated surface thickness distribution for a CMC type- I orientation. There is an increase in Nusselt number with the increase in thickness elevation near the wall jet region. Due to superimposing effect of the weave pattern and transition region, distinguishing the exact effect of the weave pattern is difficult. Further, the computational data shows comparatively smooth enhancement because the surface simulated in computational model, is the high-resolution model (as measured by Ricklick, 2015) with no steps due to resolution of 3D printer. The computational data shows no high peaks but it is difficult to relate the effect of thickness on Nusselt number distribution, due to the small changes in Nusselt number. The computational data show the same trend, but the magnitude is mismatched.

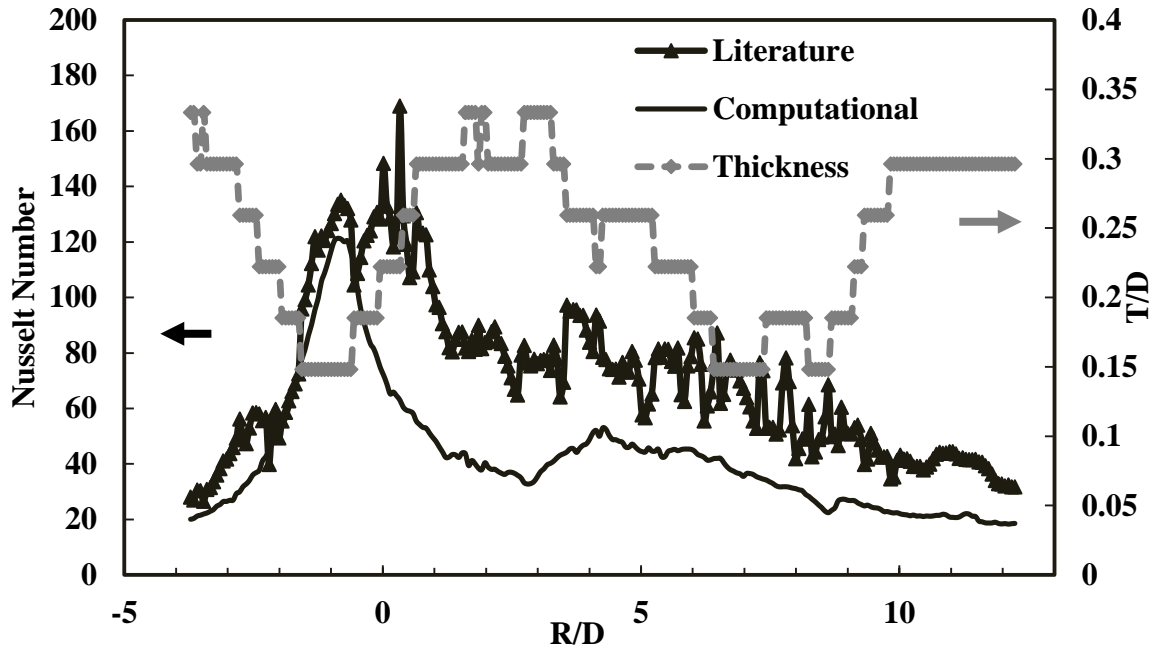


Figure 3.9: Local effect of surface waviness

3.2.4. Benchmarking Average Nusselt Number

A comparison of area averaged Nusselt numbers for the computational and experimental (Ricklick, 2015) results for 45° angled jet impingement over the test surfaces are showed in Fig. 7.3. The area considered to average the local result is shown in Fig. 3.2. It can be observed that the Nusselt number does not change much for the computational results for the range of Reynolds numbers tested. The heat transfer rates are higher for the CMC- I than the smooth surface impingement case, and smooth impingement case is higher than the CMC- II case. But, these changes are very small. Although, the v^2/f model tend to predict the trend of the local heat transfer rates for CMC impingement case in stagnation region. It has little effect on the area averaged Nusselt number because this area averaged majorly comprises the stagnation region; where the local trend follows that of a smooth case. Hence, the area averaged Nusselt number for CMC- I, CMC –II and smooth impingement cases almost remain the same. As expected the average heat transfer rates

increases with increase in Reynolds number, for the computational results. This turbulence model predicts the average Nusselt number for smooth impingement case better than the CMC- I and CMC- II case, with an error of 17.87% and 34.9% for Reynolds number 11,000 and 23,000 respectively. The error in predicting the average Nusselt number also increases with increase in Reynolds Number as expected. As the average Nusselt number for the computational results for smooth, CMC- I and CMC- II remains the same, but the experimental results show increase in heat transfer rates in case of CMC- I and CMC- II. Hence, the error in predicting the area average Nusselt number for CMC- I and CMC- II for this computational approach are high and in the range of 30-49%.

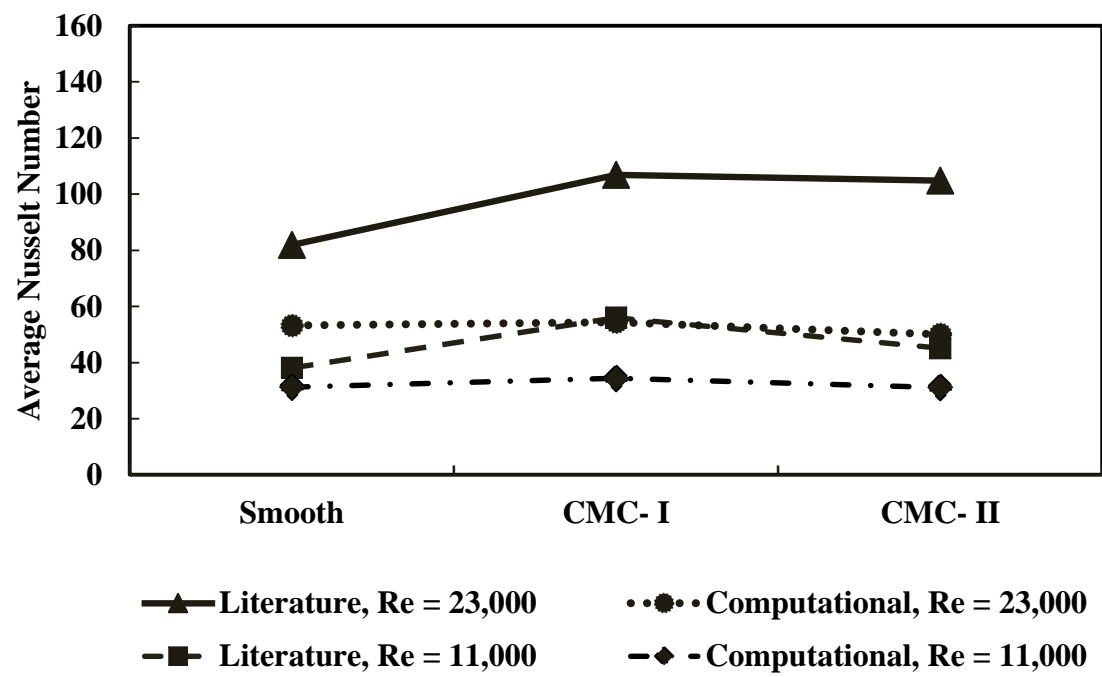


Figure 3.10: Area averaged Nusselt number at H/D= 6.5 and $\phi = 45^\circ$

4. Jet Impingement Experimental Study

As discussed in the literature, Ricklick (2015) experiments were conducted on a low-resolution 3D printed sCMC surface causing high uncertainties in the results. Hence in this experimental study, high resolution sCMC surface is investigated for average heat transfer rates under air jet impingement cooling with reduced uncertainties discussed below.

4.1. Methodology

The aim of this investigation is to obtain accurate heat transfer coefficients and to estimate the effect of a simulated CMC surface on heat transfer rates. The most important and distinctive feature affecting the heat transfer characteristic is the surface profile of the CMC; hence, detailed representation of this profile is important in this study. For accuracy and surface finish Computer Numerical Control (CNC) machining was selected. A sample of the machined part can be seen in Fig. 4.1, which was machined from the previously collected surface profile data (Ricklick, 2015). The sample was machined using a 19mm thick aluminum slab, and the accuracy of the CNC machine is approximately 10times more than that of the 3D printer used by Ricklick (2015). Comparing the Figs 4.1 and 4.2, the difference between the CNC machined surface and 3D printed surface can distinguished. The wavy nature of the surface can be seen with smooth curvature on aluminum surface, which was not available in the 3D printed part. The low-resolution steps of plastic laid out by the printer is visible in 3D printed CMC.



Figure 4.1: CNC machined CMC simulated surface

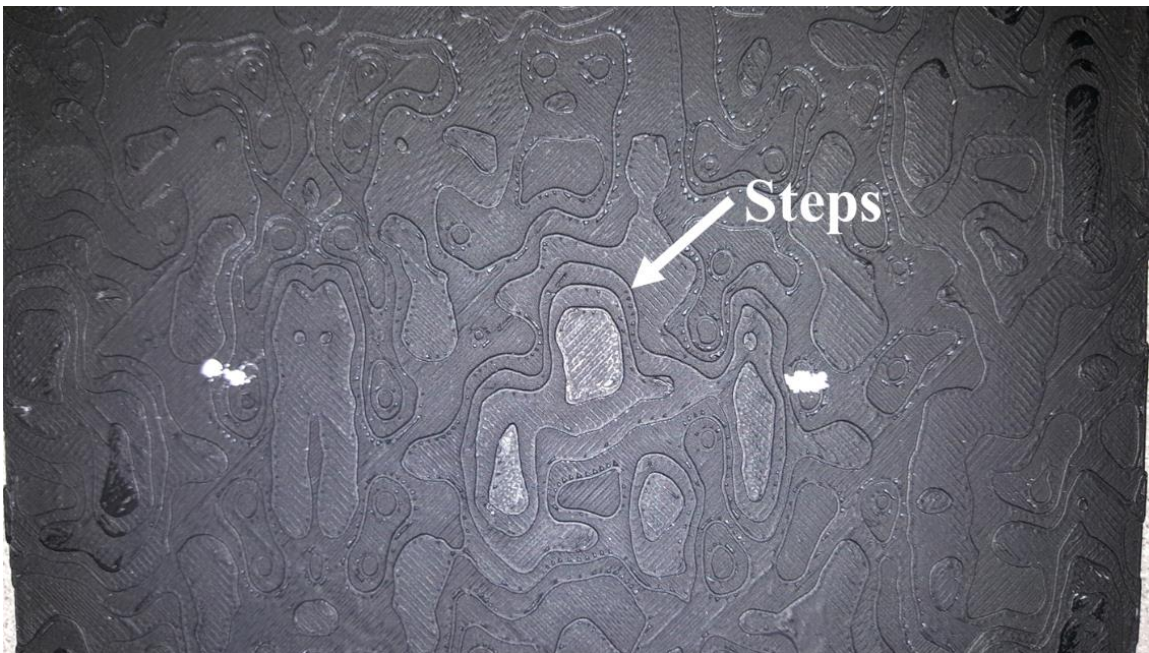


Figure 4.2: 3D printed low resolution CMC surface (Ricklick, 2015)

Average heat transfer rate is determined from the temperature difference between the air jet and surface temperature of the sCMC surface. A constant surface temperature at all local points is assumed and temperature is measured at three distinct points along the diagonal of the square sCMC surface. This assumption of equal local temperature on the surface can be attained by having a high conductive heat transfer rate compared to the convective heat transfer rate at this surface. This assumption can be proven if the ratio of conductive resistance to convective resistance also called Biot number, is much less than 1. The Biot number is given by the equation 5. The Biot number is proportional to the conductivity of the material and heat transfer coefficient. Hence, high thermal conductive aluminum is used to machine the CMC surface. The cross-sectional area of conduction (A_{cond}) is inversely proportional to the Biot number. Hence, the thickness of the sCMC surface plate was not able to render a low Biot number, therefore the sCMC plate was extended by attaching an aluminum plate of 12.7mm to decrease the Biot number. The Biot number was calculated to be less than one, hence a constant temperature on the surface can be assumed.

$$Bi = \frac{h L_c A_{conv}}{k_{Al} A_{cond}} \quad (5)$$

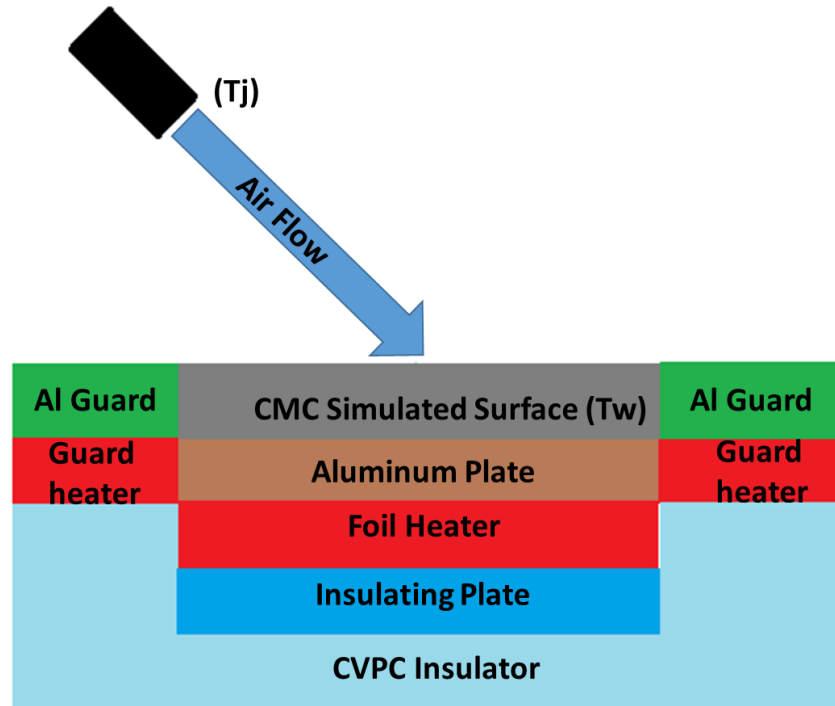


Figure 4.3: Schematic of Experimental Set-up

A sketch representing the experimental methodology is shown in Fig. 4.3. A foil heater is placed on the back side of the extended sCMC surface to provide a heat flux. The effective heat flux flowing through the simulated surface is calculated by measuring the current flowing through the heater and it is calibrated by a heat leakage test. The surface temperatures of the sCMC is measured using type-T thermocouples, at three distinct points and then averaged. Due to low Biot number of the surface the temperature difference measured between these points was less than 1°C . To avoid heat loss from the side of the surface, guard heaters are placed on each side and maintained at a temperature equal to CMC surface temperature. To reduce heat loss from the back of the heater, CPVC insulating material is placed. For validation, the sCMC surface is replaced by a flat plate and results are compared against the correlation of Martin (1977).

The heat transfer coefficient can be calculated using Newton's law of cooling with this known effective heat flux and temperature difference between the surface and the jet. The average Nusselt number is calculated from the heat transfer coefficient. Detail method of calculating the average Nusselt number is elaborated in the experimental data reduction section.

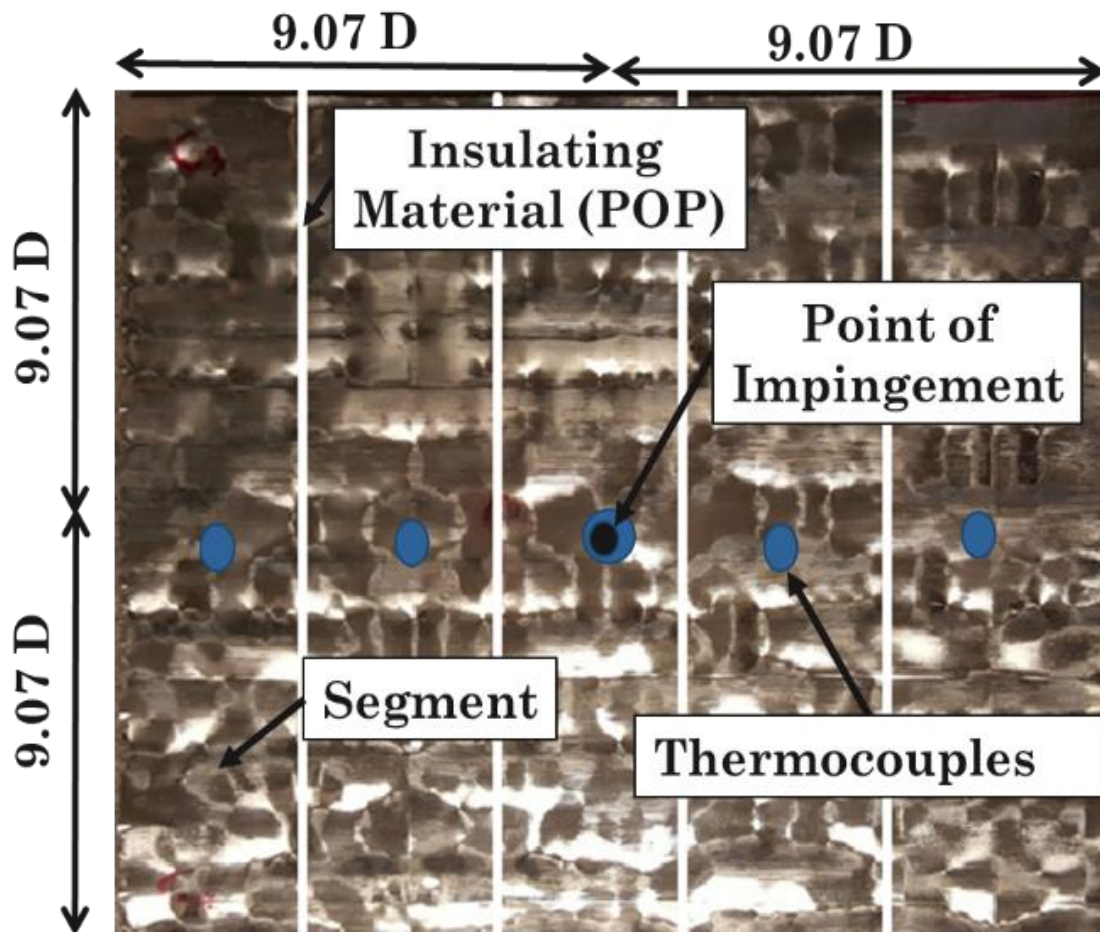


Figure 4.4: Segmented CMC simulated surface

The assumption of uniform surface temperature can further be scrutinized by the segmented approach, where the surface is broken down into five segments in the main weave direction as shown in Fig. 4.4. These segments are separated by 1mm thick insulator

(POP, $k \sim 0.17 \text{ Wm}^{-1}\text{K}^{-1}$) to avoid lateral conduction. These segments are heated using individual foil heaters to maintain a constant equal temperature between them and their respective effective heat flux is measured. Individual temperature of the segmented surfaces is measured using thermocouples and average Nusselt numbers are calculated as before for each segment. Further, the overall Nusselt number is determined using the mean surface temperature of the segments and overall heat flux supplied to the heaters.

4.2. Experimental Setup

The main components of the experiment are illustrated in Fig. 4.5. The setup mainly constitutes a metered air supply coming from compressed air line through an airflow meter, this air is then supplied into a Cylindrical plenum of 25.4mm diameter. The air supply was measured using a rotameter, the accuracy of the meter was 0.2 scfm. The length of plenum measuring 597mm was used to ensure uniform flow approaching the orifice (Yan, 1997). This plenum consists of honey comb and steel wool at the inlet, to baffle and condition the flow. The honeycomb used had cell size of 6mm and the length was 12 times the cell size (Mehta, 1979). At the exit of this plenum, an orifice measuring 7mm was placed with an orifice length much less than 1 diameter to ensure uniform velocity (Shakouchi, 2012). The jet orifice was positioned at 7 jet diameters from the surface, at an angle of 45° from the horizontal. Initially, these experimental parameters were selected to match Ricklick (2015) literature to validate results. Due to the difference in area averaged, Martin (1977) correlation was used to validate the experimental results. Error estimation showed an error in stagnation Nusselt number of 15.2%, the major error contributed is due to the uncalibrated thermocouple, which was in the range of $\pm 1^\circ\text{C}$.

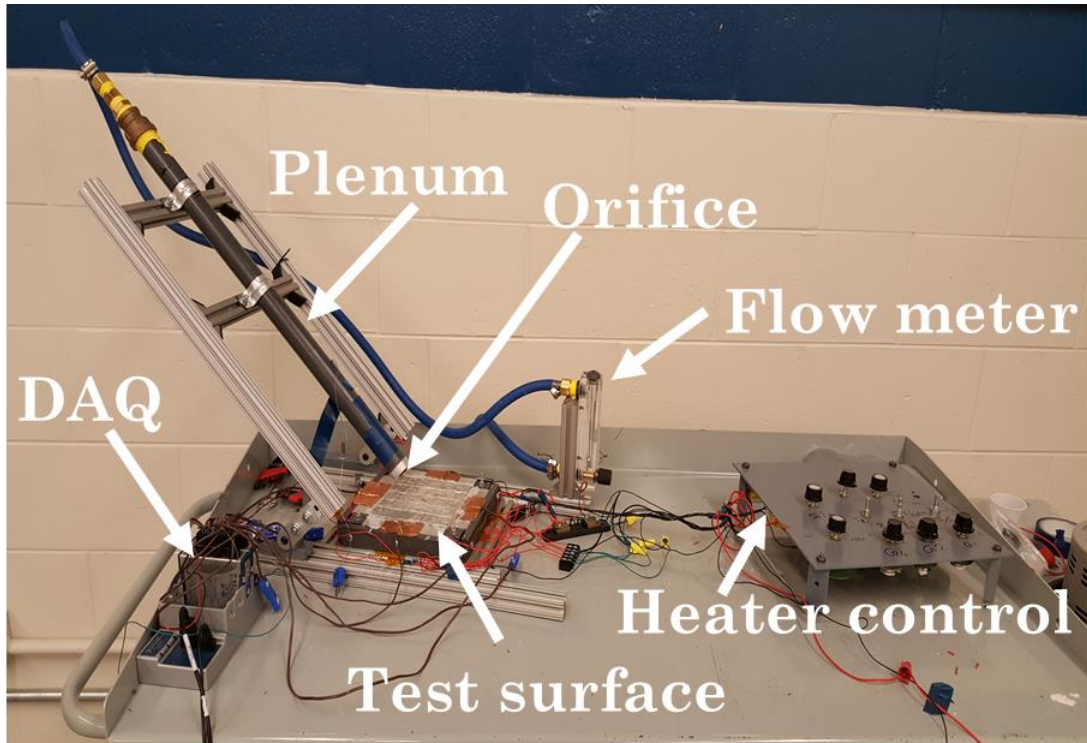


Figure 4.5: Experimental setup

4.2.1. Experimental Heat Leakage Test

The accuracy of the result is a function of the measured heat flux, any heat loss from the simulated surface should be accounted. Generally, heat leakage test is carried out by placing insulating material on the heat transfer surface such that one can assume the generated heat leaks through the sides and the back of the experimental rig.

This insulator is replaced by guard heaters on each side of the surface where there is heat loss as shown in Fig. 4.6. The temperature of the guard heaters is measured and controlled using potentiometers, at a constant temperature equal to the temperature of the specimen. This constant temperature boundary condition on each surface is a better approximation than placing an insulator on this surface.

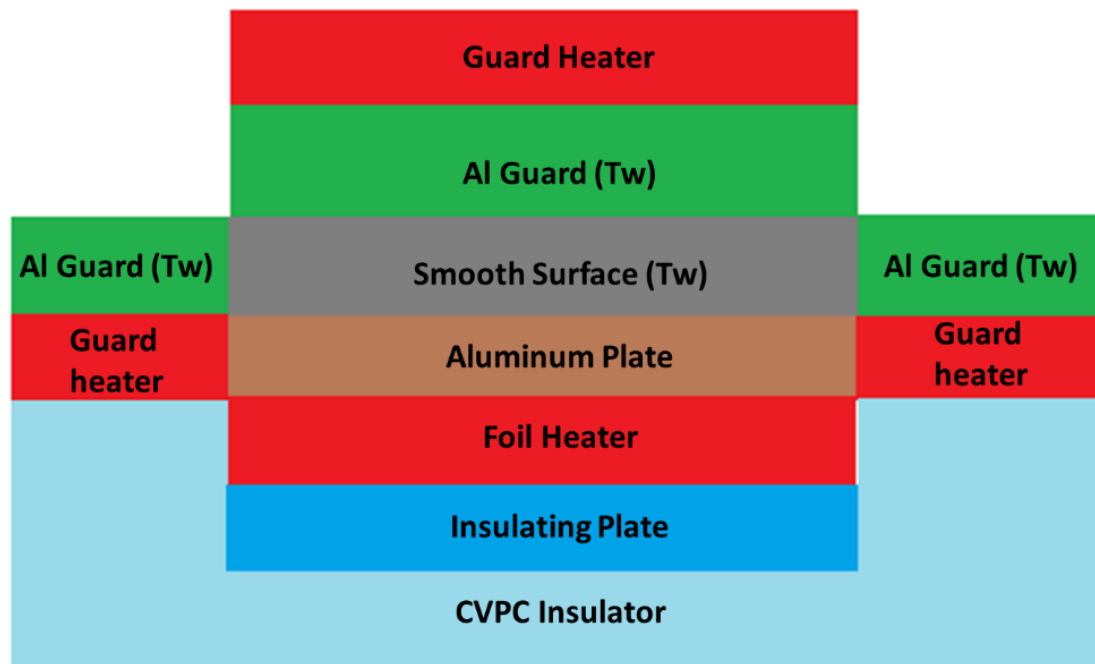


Figure 4.6: Heat leakage setup (Cross-sectional view)

The specimen tested was surrounded by heaters in all directions as shown in Fig. 4.6. As the temperature difference between the guard heaters and the specimen is zero, from Fourier law of conduction it can be proved that the heat transfer is also equal to zero. Hence, heat loss occurring should be driven in the backward direction from the foil heater.

A low conductive material (CVPC) was kept at the back of the foil heater, the surface temperature on both top and bottom of this plate were measured. Three thermocouples were placed on each surface and found to be having equal temperature within ± 1 Celsius, which is allowable under the error of the type-T thermocouple of ± 1 Celsius. The heat lost from the back of the foil heater is flowing through this plastic plate.

Assuming 1D conduction and knowing the surface temperature, heat flux and thickness of the plate; thermal conductivity of this material can be calculated using

Fourier's law of conduction (equation 6).

$$q_{loss} = -k_{CVPC} * A_{CVPC} * \frac{\Delta T}{t_{CVPC}} \quad (6)$$

The heat leakage experiment was carried out for one heat flux and corresponding temperature difference of the surface temperature and the room temperature versus the heat loss is shown in Fig. 4.7. A straight-line function was also determined to fit this curve shown in Eq 7.

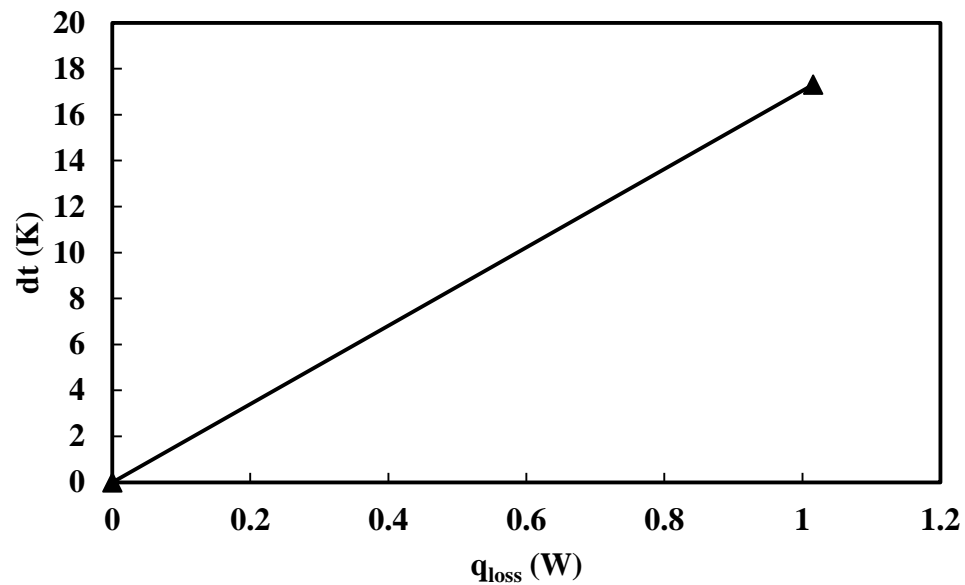


Figure 4.7: Heat loss versus change in temperature

$$q_{loss} = \left(0.05869 \frac{W}{K}\right) \Delta T \quad (7)$$

The heat loss from the foil heater was determined, and as sanity check the thermal conductivity of CPVC was measured to be $0.136 \text{ Wm}^{-1}\text{K}^{-1}$ and compared to the published value. The error between the published value and measured value was found to be 2.82%. Hence, this process of calculation can be reversed to find the heat loss using the measured thermal conductivity. Hence, in this current study heat lost is found using this conduction method and the measured thermal conductivity of the plastic plate.

4.2.2. Experimental Data Reduction

The total heat flux supplied to the heater is calculated using the Eq. 8, by measuring the resistance and current flowing in the resistive foil heater. The effective heat flux flowing through the test specimen is given by Eq. 9.

$$q'' = \frac{I^2 R}{A_{Conv}} \quad (8)$$

$$q''_{eff} = q'' - \frac{q_{loss}}{A_{CVPC}} \quad (9)$$

Heat transfer coefficient is determined using the calculated effective heat flux and measured temperature difference between the air jet and test surface. The heat transfer coefficient formula used is shown in Eq. 10.

$$h = \frac{q''_{eff}}{T_w - T_j} \quad (10)$$

The Nusselt number is calculated using the Eq. 11. The characteristic diameter (D) used in this formula is the diameter of the orifice selected in this study.

$$Nu = \frac{h D}{k_f} \quad (11)$$

The Reynolds number was calculated using the measured mass flow rate from the rotameter. The diameter (D) and area (A_o) used in this equation is the diameter of the orifice and the area of the orifice diameter respectively.

$$Re = \frac{\rho \dot{m} D}{\mu A_o} \quad (12)$$

In the segmented approach, average Nusselt number for individual segment is calculated using the above equation 10 and 11 in the same method, but the heat flux is replaced by individual heat flux to find the individual Nusselt number. The formula used to calculate the individual heat flux is given by,

$$qi''_{eff} = qi'' - \frac{q_{loss}}{5 * A_{CVPC}} \quad (13)$$

$$i = 1 \text{ to } 5$$

The overall average Nusselt number for segmented approach is calculated from the overall summation of individual heat flux given by Eq. 14.

$$q''_{eff} = q1'' + q2'' + q3'' + q4'' + q5'' - \frac{q_{loss}}{A_{CVPC}} \quad (14)$$

4.3. Experimental Results

The area of impingement surface averaged is represented with dimensions in the Fig. 4.8, by reference to the geometrical point of impingement.

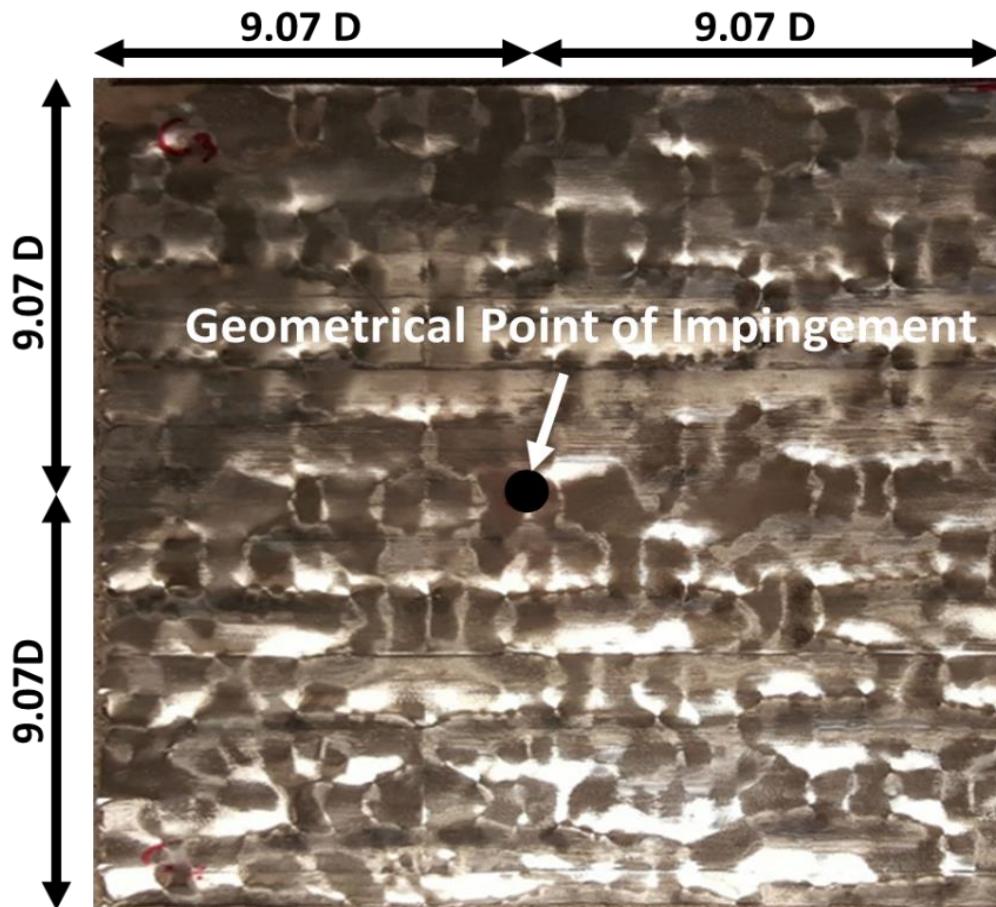


Figure 4.8: Experimental test specimen

4.3.1. Experimental Result Validation

The smooth surface impingement, experimental results were compared to the values obtained from the correlation (Eqs 1&2) Martin (1977) provided in his summarized literature review. The heater plate used in the literature is circular in shape, but in this current study the heater surface is a square. The heater radius as a limit of 2.5 to 7.5D. In this study, the length between the edge of the plate and the point of impingement is 9.07 jet diameters. Hence, the average value from the correlation is calculated for a heater radius of 7.5 jet diameter and a Prandtl number of 0.713 at atmospheric temperature of 300 Kelvin

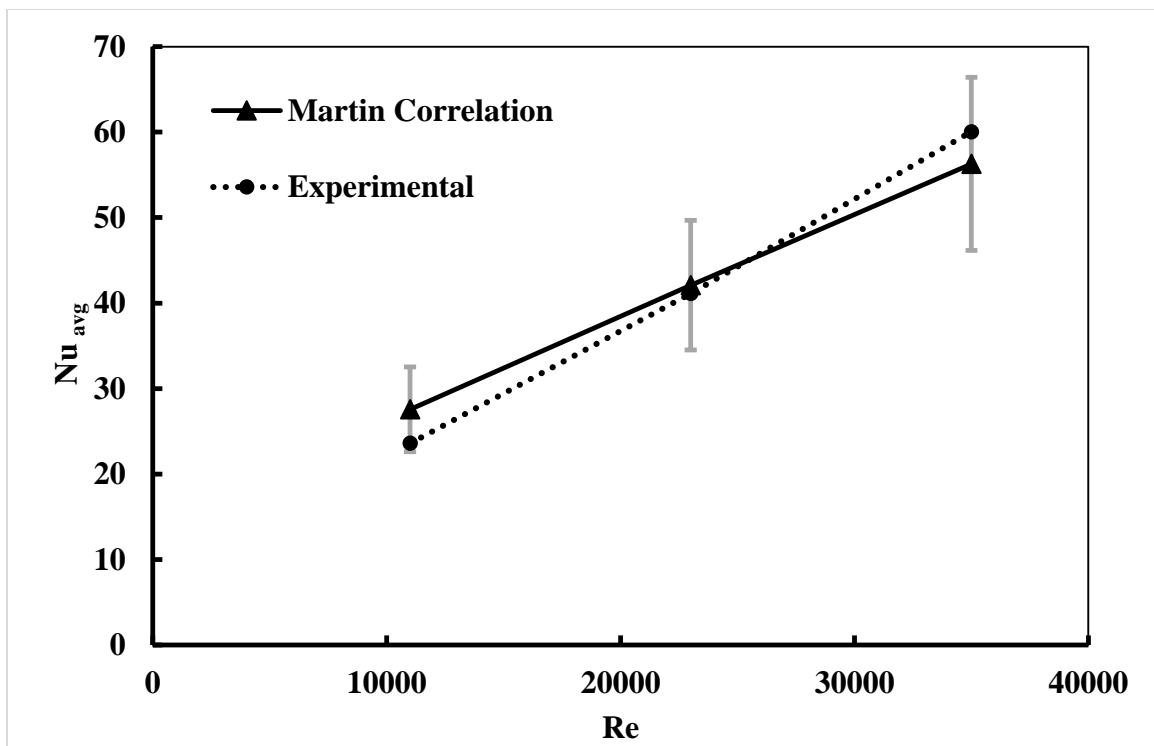


Figure 4.9: Comparison of average Nusselt number against literature

Experimental results for normal jet impingement over smooth surface for an H/D of 7 jet diameters, $\phi = 90^\circ$ and for Reynolds number range of 11,000 to 35,000 is shown in Fig. 4.9. It can be observed that the experimental and literature results are close to each

other and a maximum error of 14.4% is present between the experimental and the literature value at a Reynolds number of 11,000. It is conjecture that the error is due to the difference in heater area. Summarizing these result, it can be concluded that the errors obtained for experimental results are acceptable.

4.3.2. Individual Segment Average Results

The individual segment average results for the two orientation are plotted for the segmented CMC simulated surface shown in Fig. 4.4. As discussed, the whole domain is broken down into five segments in the main weave direction. Hence, these segments fragmented are in the perpendicular direction towards the streamwise direction, for CMC-II orientation and in parallel direction towards the streamwise direction, for the CMC-I orientation. These two orientation of segmentation are shown in Figs 4.10 and 4.11 below.

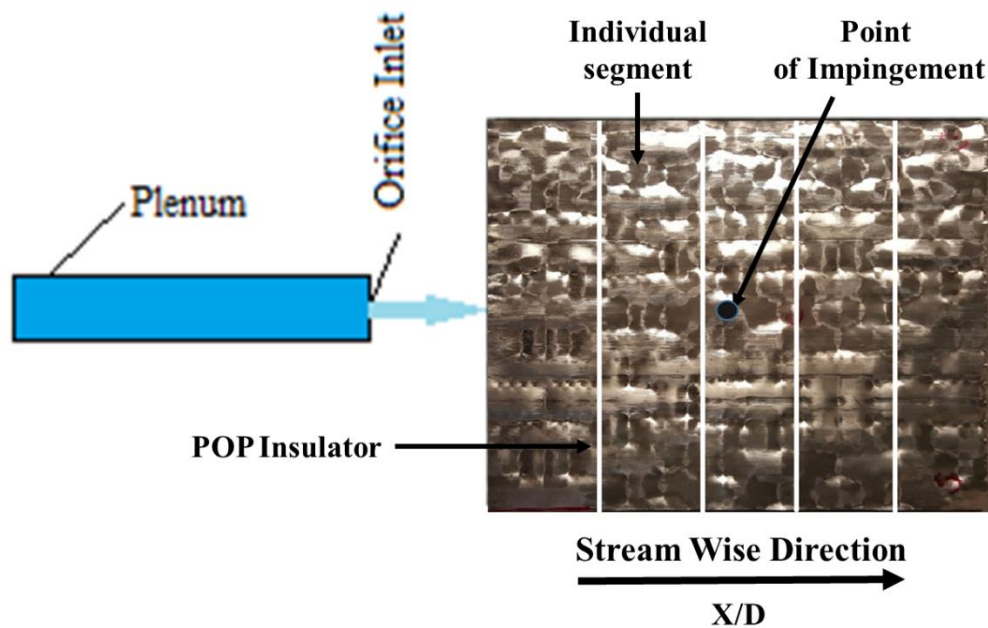


Figure 4.10: Segmented CMC- I orientation

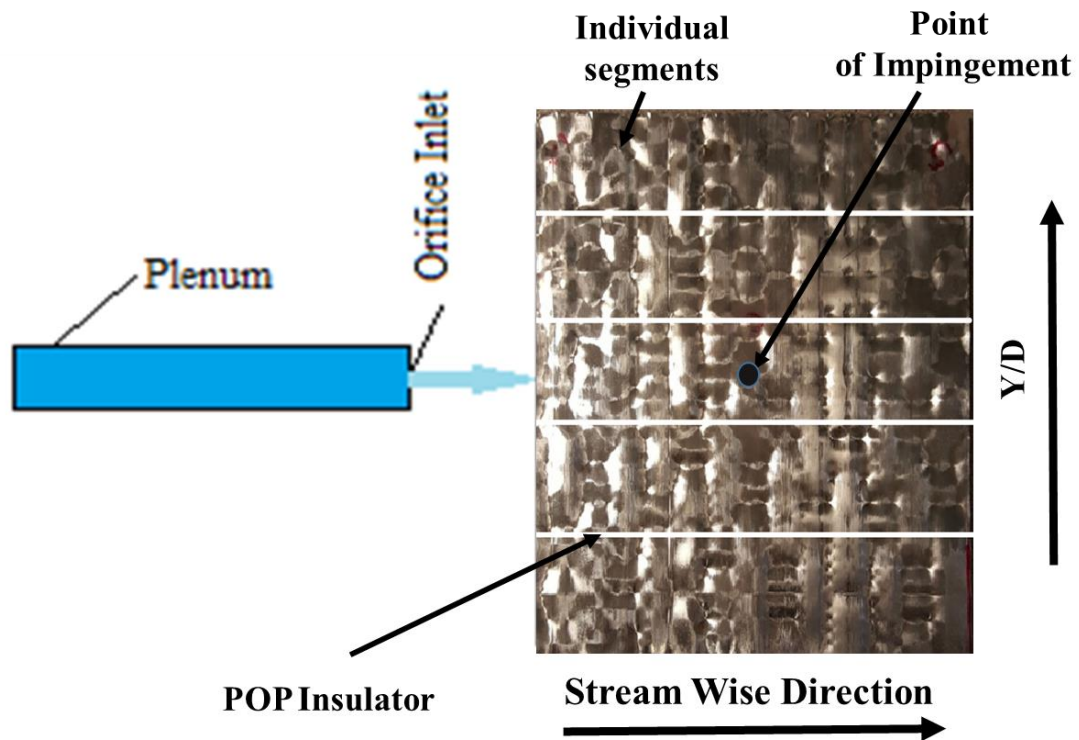


Figure 4.11: Segmented CMC- II orientation

Individual segment average results for CMC normal impingement ($\phi = 90^\circ$) case, at H/D of 7 and Reynolds number of 11,000 to 35,000 are shown in Fig. 4.12. The normal impingement case (CMC- N) is tested in the segmented CMC-II orientation. As expected, segmented average Nusselt number increases with the increase in Reynolds number. The trend of local values remains the same on either side of point of impingement, and the change in Nusselt number with Reynolds number is higher in the stagnation region and consecutively decreases in the wall jet region.

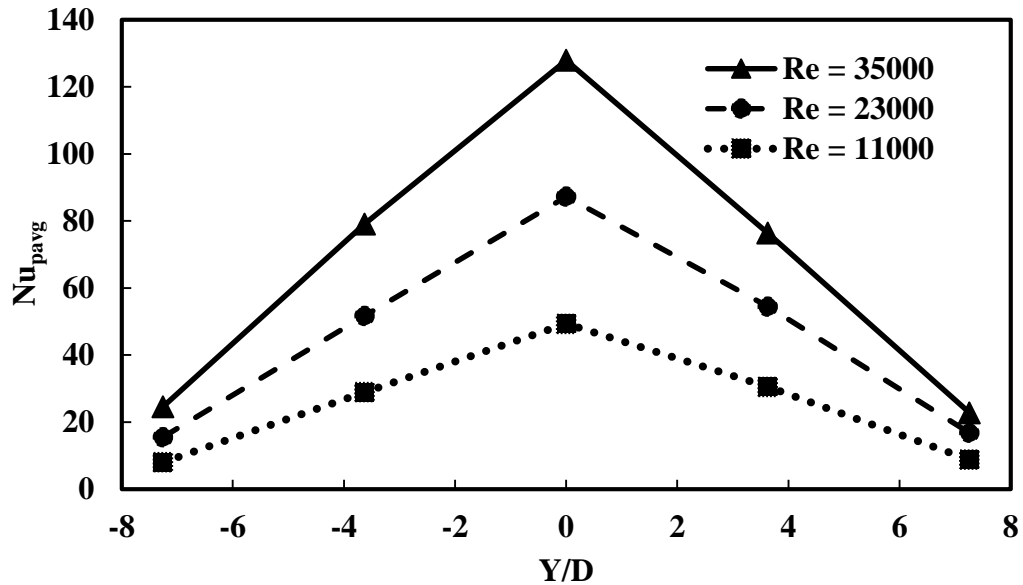


Figure 4.12: CMC- N ($\phi = 90^\circ$) impingement case, individual segment average Nusselt number

Similarly, segmented average results for a CMC-I oblique jet impingement at a H/D of 7, $\phi = 90^\circ$ and for a Reynolds number range of 11,000 to 35,000 are shown in Fig. 4.13 below. The segmented average results for this CMC-I impingement case is in stream wise direction (X/D). CFD results from local plot for a CMC-I in Fig. 3.7, showed the formation of secondary peak at R/D of 4.1 jet diameters. This secondary peak causes higher average values at a R/D of 3.62, which can be observed in the figure. Average heat transfer rates in downstream side is comparatively higher than the value in upstream side, due to the secondary peak in the downstream direction. This increase claims that, there are higher turbulence level in downstream direction than the upstream direction.

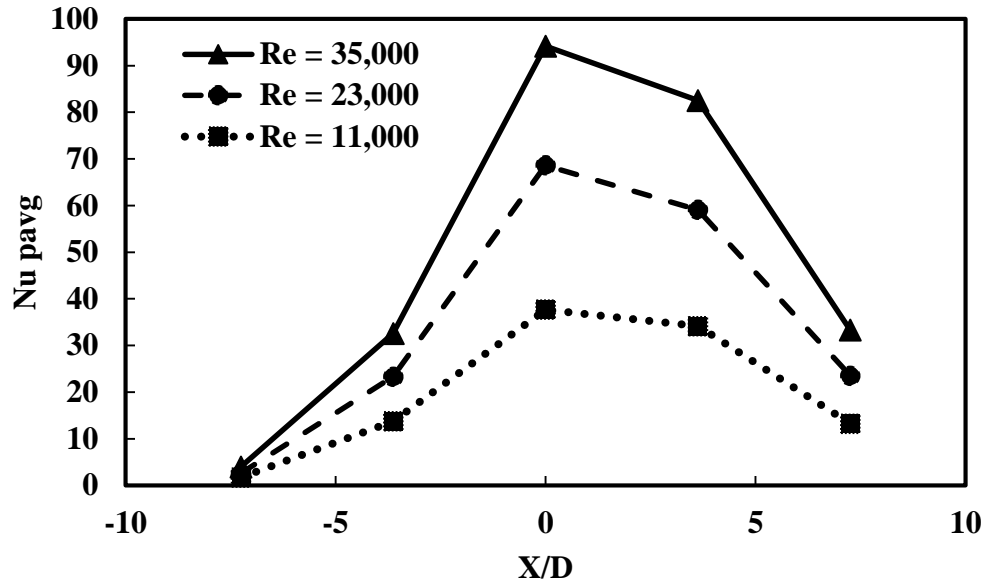


Figure 4.13: CMC- I impingement case, individual segment average Nusselt number

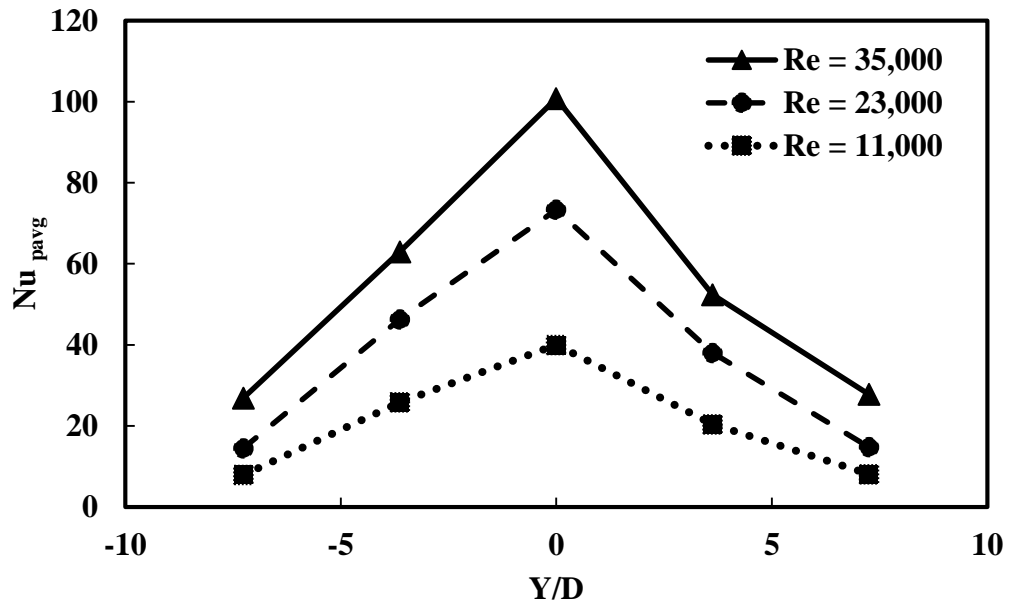


Figure 4.14: CMC- II impingement case, individual segment average Nusselt number

Figure. 4.14, represents the average results for a CMC- II oblique impingement case at a H/D of 7, $\phi = 45^\circ$ and for a Reynolds number range of 11,000 to 35,000. These results are plotted in the spanwise wise direction (Y/D); therefore, distribution of local heat

transfer rates is uniform on either side of the jet impingement point. Local values on the right is slightly higher than the values on the left, this can be caused by uncertainty or the position of geometrical point of impingement or both.

To compare the effects of waviness on local average Nusselt number, local values for CMC-I, CMC-II and CMC-N for a Reynolds number of 35,000 are shown in Fig. 4.15. The experimental parameters are H/D of 7, for CMC-I and CMC-II angle of jet impingement of $\phi = 45^\circ$ and CMC-N is normal jet impingement ($\phi = 90^\circ$). Due to difference in segmenting orientation about the streamwise direction for CMC-I and CMC-II, segmented average results cannot be compared. Hence, CMC-N is used as a baseline for both the orientations. Comparing CMC-I and CMC- N, stagnation region average result show 35% higher heat transfer rates for CMC- N. For CMC-II and CMC-N, CMC-N shows 26.9% higher average result than CMC-I. CMC-N performs better than CMC-I and CMC-II because local values are distributed equally on downstream and upstream of the flow, whereas for CMC-I and CMC-II, it is oblique impingement with the secondary peak in the downstream direction. This results in higher heat transfer rates in downstream direction but in this study, only a part of this area is considered to average local Nusselt number due to dimension constraints.

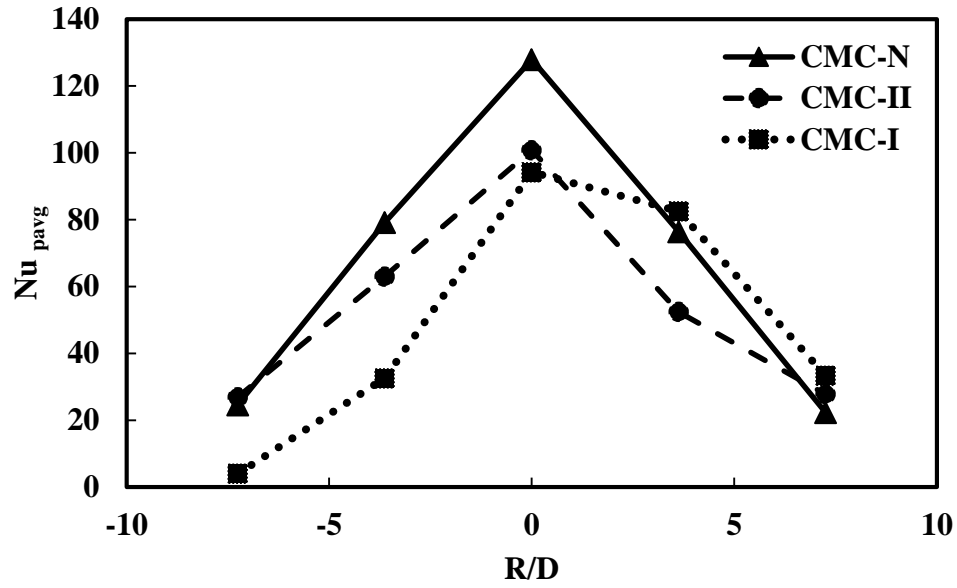


Figure 4.15: Comparison of pseudo average Nusselt number at $Re = 35,000$

4.3.3. Area-Averaged Nusselt Number

Comparing the effect of CMC over a smooth surface for a normal impingement case ($\phi = 90^\circ$) at H/D of $7D$ and Reynolds number range of $11,000$ to $35,000$. The Fig. 4.16 shows the average Nusselt number for the range of Reynolds number tested. It can be observed that there is an increase in Nusselt number for the CMC surface. This increase in Nusselt number is proportional to the increase in Reynolds number. The maximum percentage change is 12.5% for Reynolds number of $35,000$, but still in the uncertainty band of the experiment. The segmented experimental results are very close to non-segmented experimental results as expected. The maximum error between segmented and non-segmented result is equal to 2.9% , which is less than the uncertainty of the experiment.

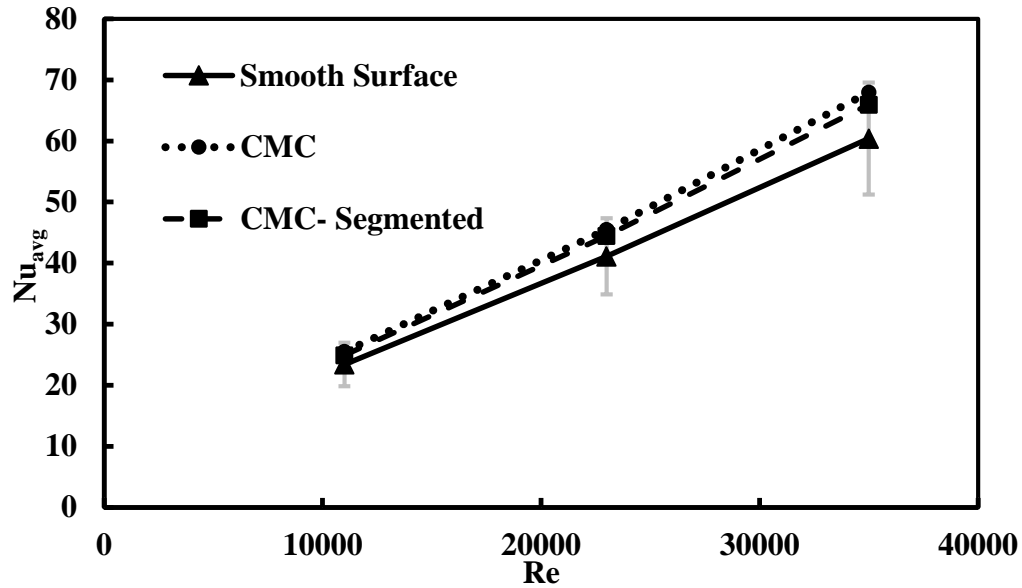


Figure 4.16: Comparison of area averaged Nu for normal ($\phi = 90^\circ$) impingement case

Area averaged experimental results for an oblique jet impingement on a CMC surface are shown in Fig. 4.17. The average Nusselt number for various impingement cases are plotted for their respective Reynolds number. The parameters for these results are H/D of 7, $\phi = 45^\circ$ and a Reynolds number range of 11,000 to 35,000. Comparing CMC-I and CMC- II orientation results, CMC-II orientation augments heat transfer rates further than the CMC- I orientation. The increase in Nusselt number is in the range of 10.8-14.9%. This increase in Nusselt is proportional to the increase in Reynolds number. This contradicts the average experimental results of Ricklick (2015) discussed in the literature. This is because the CMC surface simulated in this study is high resolution smooth curvature surface as compared to the low-resolution 3D printed surface used by Ricklick. Another factor contributing to this difference is the area over which the Nusselt number is averaged. The literature considers larger area in the downhill side, and in this study, equal areas on the uphill and downhill direction are considered to determine average result. As the local

Nusselt number in the downhill direction is always higher than the local values in the uphill direction, these experimental values are less than the average values of literature (Ricklick).

Comparing smooth surface and CMC surface results, smooth surface is performing better than the CMC-I orientation, and CMC-II orientation is leading the smooth surface results marginally in heat transfer rates. Although there is an increase in Nusselt number in the range of 15%, this is within the experimental uncertainty.

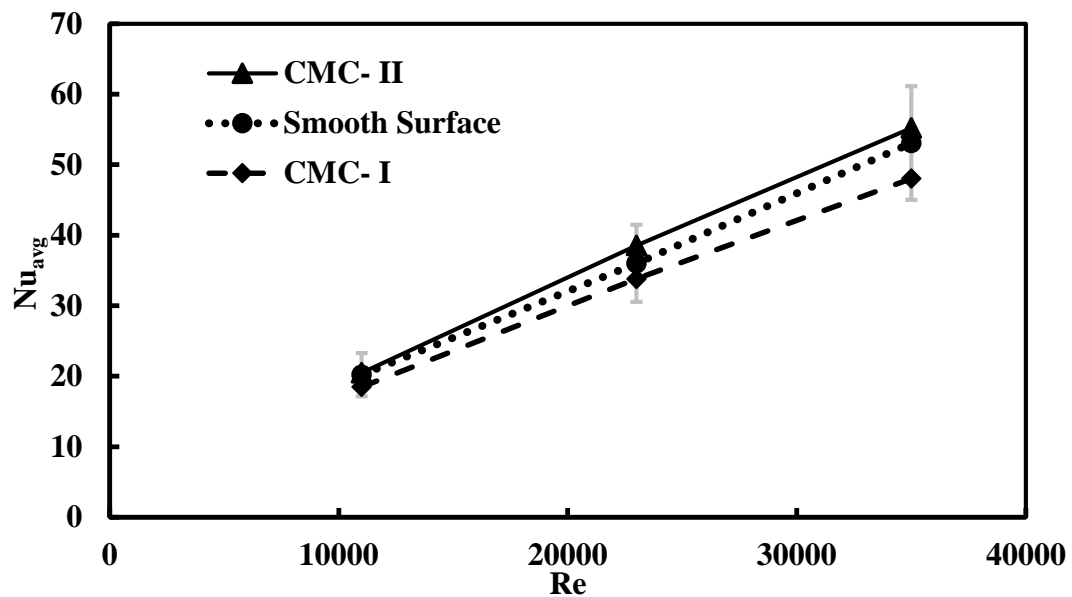


Figure 4.17: Comparison of area averaged Nusselt number at $\phi = 45^\circ$

To determine the effect of segmented and non-segmented CMC surface, area averaged Nusselt numbers for these cases are plotted in the Fig. 4.18 at H/D of 7 and $\phi = 45^\circ$. Results show that the segment average values closely match the non-segmented results with a maximum error of 8%, and this error lies within the uncertainty band of the experiment.

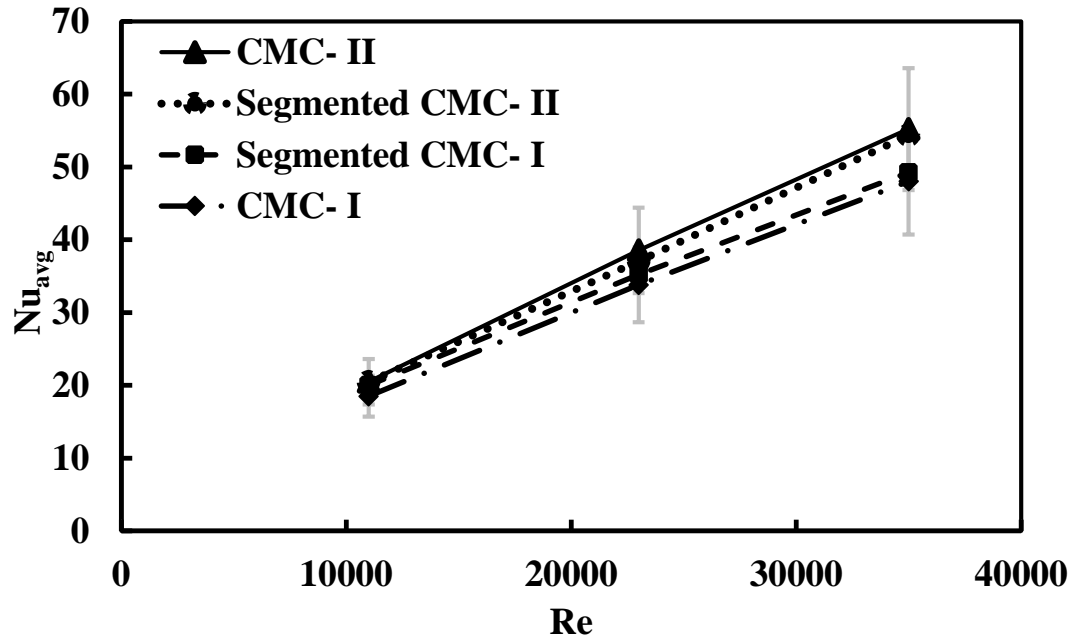


Figure 4.18: Comparison of average Nu for segmented and non-segmented CMC surface at $\phi = 45^\circ$

5. Experimental Result Benchmarking Study

5.1. Computational Setup

The computational domain was setup matching the current experimental test parameters. The domain was setup like the previous approach discussed in the jet impingement literature benchmarking study (Section 3) and with the same mesh characteristics. Hence the mesh generated, produces mesh independent results. The domain of the solid sCMC represented in this study is smaller in length as shown in Fig. 4.8. In this setup, the bottom wall is given a constant heat source instead of the constant temperature, matching the condition of the experimental methodology. The physical properties of this domain are listed in the table 5.1. Data reduction was carried out using the same procedure discussed in the previous benchmark study

Table 5.1: Physical Properties of the mesh domain

Description	Values
Atmospheric temperature (K)	$T_{\infty} = 300$
Atmospheric pressure ($\text{kgm}^{-1}\text{s}^{-2}$)	$P_{\infty} = 101325$
Density of air (kgm^{-3})	$\rho = 1.18415$
Dynamic viscosity of air ($\text{kgm}^{-1}\text{s}^{-1}$)	$\mu = 1.855 \times 10^{-5}$
Jet diameter (m)	$D = 0.007$
Non-dimensional nozzle to plate distance	$H/D = 7$
Heat flux at bottom wall (W)	$q = 50$
Temperature of impinging jet (K)	$T_j = 300$
Thermal conductivity of fluid air ($\text{Wm}^{-1}\text{K}^{-1}$)	$k_f = 0.0260305$
Thermal conductivity of solid ($\text{Wm}^{-1}\text{K}^{-1}$)	$k_{Al} = 167$

5.2. CFD Results

Segmented average and area averaged numerical results are benchmarked against the experimental results. The region used for the area averaged for the area-averaged results is shown in Fig. 4.8.

5.2.1. CFD Results Validation

The smooth surface impingement, computational results were compared to the values obtained from the correlation (equation 1&2) Martin (1977) provided in his summarized literature review. The average value from the correlation is calculated for a heater radius of 7.5 jet diameter and a Prandtl number of 0.713 at atmospheric temperature of 300 Kelvin. Similarly, CFD local Nusselt numbers for the area of heater radius are averaged and compared. Computational and literature results for normal jet impingement over smooth surface is shown in Fig. 5.1 below, for a H/D of 7 jet diameters, $\phi = 90^\circ$ and for Reynolds number range of 11,000 to 35,000. Comparing computational and literature results, the average Nusselt is predicted well by the v^2f turbulence model with a maximum error of 19.6% at Reynolds number of 35,000. This error is acceptable since it is close to the literature result uncertainty of $\pm 18\%$. Hence the following computational results are considered acceptable.

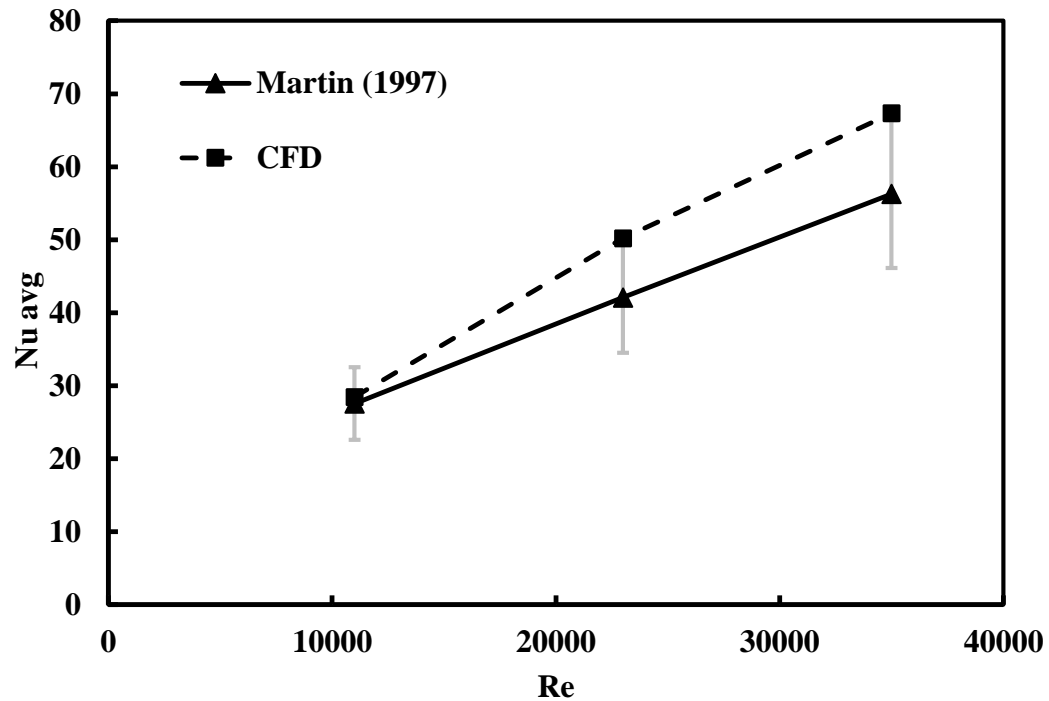


Figure 5.1: Average Nusselt number plot for computational result validation, at $H/D=7$ and $\phi = 90^\circ$

5.2.2. Benchmarking Area Average Nusselt Number

A comparison of area averaged Nusselt number for computational and experimental results for CMC- I, CMC- II and smooth surface impingement cases are shown in Fig. 5.2. The test parameters are H/D of 7, oblique angle of impingement of 45° and Reynolds number range of 11,000 to 35,000. CFD results show no considerable change in average Nusselt for the three cases tested. The v^2f turbulence model is not able differentiate between the CMC and smooth surface, as discussed in the local Nusselt number benchmarking study (section 3). This turbulence model is not able match the magnitude of Nusselt number but captures the trend. Average Nusselt predicted by the CFD for the smooth surface impingement case is in good match with the experimental values, and the error is in the

range of 14- 17%.

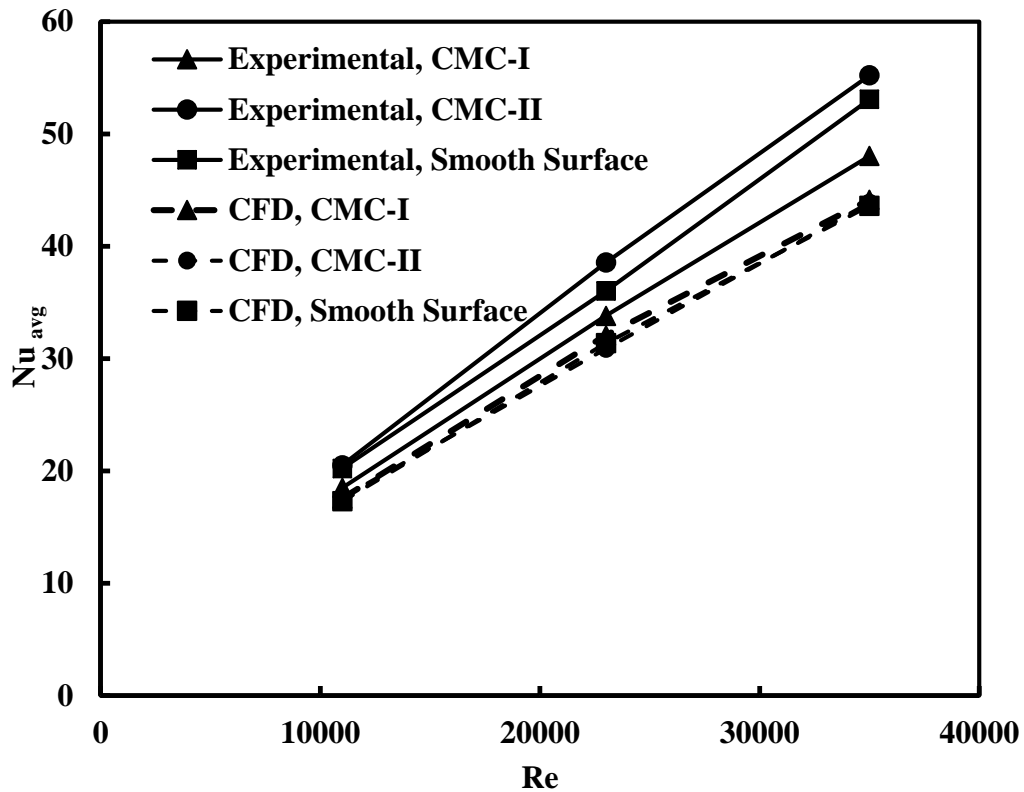


Figure 5.2: Benchmarking area averaged Nusselt number, at $H/D= 7$ and $\phi = 90^\circ$

5.2.3. Benchmarking Individual Segment Average Results

Comparing individual segment average results for CMC- I orientation, average results from simulation is averaged on each area segment matching the experimental method of averaging technique. Experiment and computational segment average results are shown in Fig. 5.3 for a H/D of 7, $\phi = 45^\circ$ and Reynolds number range of 11,000 to 35,000. Comparing local average result, CFD simulation tend to under predict the average values, the error in predicting average values is higher in wall jet region. The average result of the segment containing the secondary peak ($R/D = 3.6$), CFD result show this average value is higher than its stagnation segment but the experiment contradicts this exaggeration. The

error in stagnation region local average value, is in the range of 34.36% to 29.6%.

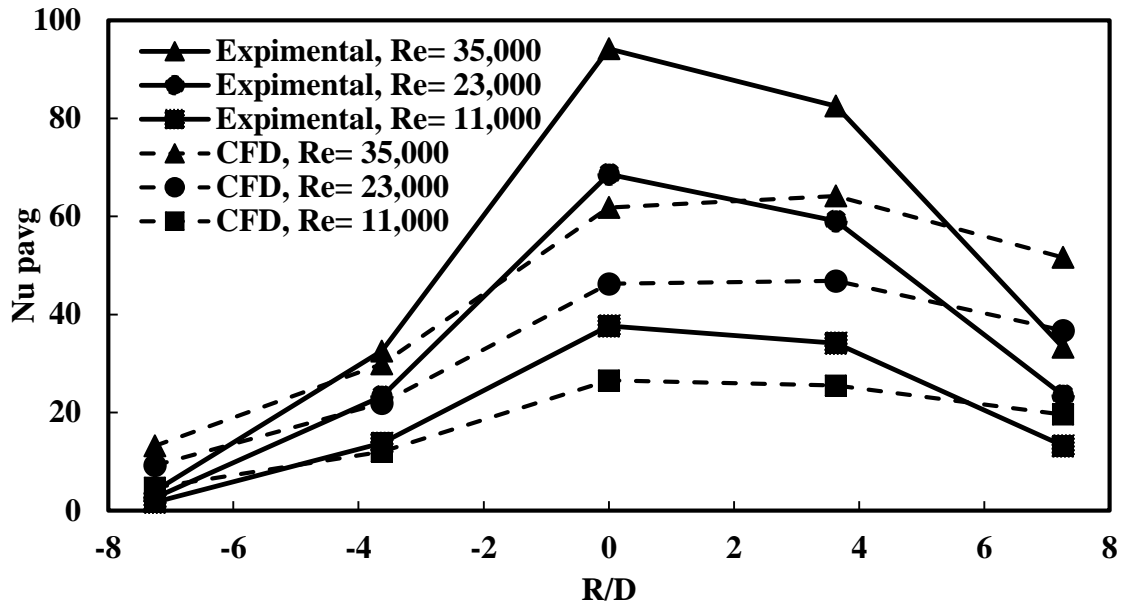


Figure 5.3: Benchmarking segmented averaged Nusselt number for CMC-I case, at $H/D=7$ and $\phi = 90^\circ$

Similarly, comparing individual segment average results for CMC- II orientation, for a H/D of 7, $\phi = 45^\circ$ and Reynolds number range of 11,000 to 35,000, shown in the Fig. 5.4. CFD results show that the average results for the end segments are in good match with experimental values. The error between the experimental and computational results is highest at the stagnation region segment. The error increases with the increase in Reynolds number, and the maximum percentage error 35% is calculated in this case study.

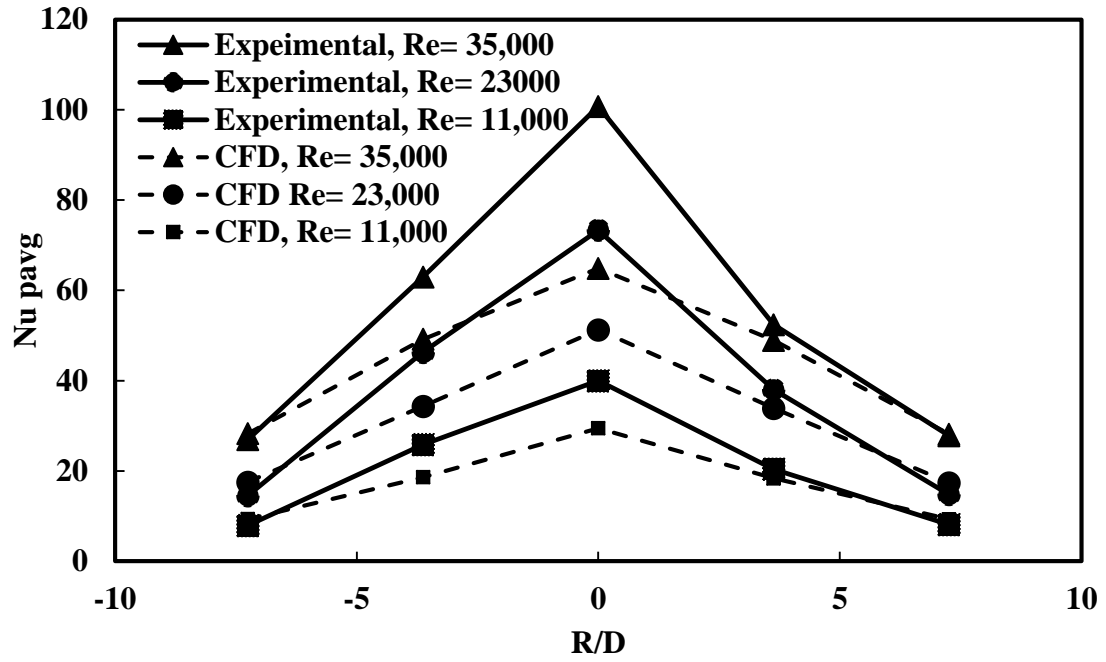


Figure 5.4: Benchmarking segmented averaged Nusselt number for CMC-I case, at $H/D=7$ and $\phi = 90^\circ$

6. Conclusion

The effect of CMC roughness on the heat transfer characteristic is studied experimentally and computationally, for Reynolds number 11,000, 23,000 and 35,000. Two types of jet impingement orientation; CMC- I and CMC- II were tested and were found that the heat transfer rates were dependent on the type of orientation. Experimental results showed the CMC surface caused a maximum augmentation in average heat transfer rates of 13%, however this lies within uncertainty band of the experiment. Hence, the effect of CMC waviness on average heat transfer rates can be neglected. The individual segment average result showed the presence of secondary peak in the downhill direction.

A constant wall temperature, segmented approach was carried to find the pseudo-local heat transfer rates and area average Nusselt number. Individual segment average Nusselt number at each segment is plotted for CMC- I and CMC- II cases, for the range of Reynolds number tested. The overall area averaged Nusselt numbers for the segmented approach matched the non-segmented experimental results with a maximum error of 8%.

For the literature (Ricklick, 2015) bench marking study, the v^2f turbulence model used, predicted the stagnation Nusselt number close to the literature values for the flat plate impingement case, and the Nusselt number decays at a faster rate than the literature values away from the stagnation region. Computational results for the CMC impingement case showed that the model produced local Nusselt number data following the same trend as that of the literature result. But the error in predicting the stagnation Nusselt number is higher than the smooth plate impingement case. The position of the secondary peak is estimated to good values. But the error in estimating the Nusselt number increases along the wall jet region. In case of CMC- II impingement case, this turbulence model fails to

predict smaller peaks.

The turbulence model predicts the area averaged Nusselt number best for a smooth impingement case with an error in range of 17.87- 34.9% and in case of CMC impingement, the error is in the range of 30-49%. But, the high uncertainty of the literature experiment results should also be considered for this large error. It can be concluded that, the v^2f turbulence model is good in predicting the impingement heat transfer rates for smooth wall air jet impingement. Whereas for a CMC surface case, this model fails to account the small rough features in augmentation of Nusselt number.

For the current experimental benchmarking study, the v^2f turbulence model can predict the area average Nusselt number close to the experimental values for smooth surface impingement case, and the error is in the range of 14-17%. But this turbulence model is not able to distinguish between the CMC and smooth surface. In case of individual segment average results, the Nusselt numbers are predicted well by the CFD near the wall jet region, and error is maximum in the stagnation region.

7. Recommendations

Future work will include investigation of the flow features and visualization of this study. Also, the effect of the geometrical point of impingement should be quantified and additional CMC parameters should be investigated, such as fiber layout, coating effects, and manufacturing effect. Augmentation of heat transfer rate by the CMC surface was observed but could not be claimed because the level of enhancement percentage was under the uncertainty band of the experiment. The percentage increase in Nusselt number increased with the increase in Reynolds number, hence higher Reynolds number ranges should be tested.

In the numerical approach, v^2f turbulence model has proved its effectiveness for smooth surface impingement cases but failed to capture the level of augmentation for the CMC impingement case. Hence, other turbulence models like LES and DNS should be evaluated to capture the augmentation over the CMC weave surface.

REFERENCES

- Auxier, T. A. (2003). *The Importance of Cooling Technology in Propulsion and Power Systems*. PRATT AND WHITNEY EAST HARTFORD CT.
- Alenezi, A., Teixeira, J., & Addali, A. (2015). Numerical Analysis of Heat Transfer Characteristics of an Orthogonal and Obliquely Impinging Air Jet on a Flat Plate. In *Proceedings of the World Congress on Engineering (Vol. 2)*. R. (2015).
- Beitelmal, A. H., Saad, M. A., & Patel, C. D. (2000). Effects of surface roughness on the average heat transfer of an impinging air jet. *International Communications in Heat and Mass Transfer*, 27(1), 1-12.
- Bischoff, M. L. (2012). *Characterization of ceramic matrix composite materials using millimeter-wave techniques (Doctoral dissertation, Wright State University)*.
- Bovo, M., & Rojo, B. (2013). Single pulse jet impingement on inclined surface, heat transfer and flow field (No. 2013-24-0003). SAE Technical Paper.
- Boyce, M. P. (2011). *Gas turbine engineering handbook*. Elsevier.
- Boyle, R. J., & Senyitko, R. G. (2005, January). Effects of Surface Roughness on Turbine Vane Heat Transfer. In *ASME Turbo Expo 2005: Power for Land, Sea, and Air* (pp. 931-942). American Society of Mechanical Engineers.
- Chakroun, W. M., Abdel-Rahman, A. A., & Al-Fahed, S. F. (1998). Heat transfer augmentation for air jet impinged on a rough surface. *Applied thermal engineering*, 18(12), 1225-1241.
- Downs, J. P., & Landis, K. K. (2009, January). Turbine Cooling Systems Design: Past, Present and Future. In *ASME Turbo Expo 2009: Power for Land, Sea, and Air* (pp. 819-828). American Society of Mechanical Engineers.
- Gabour, L. A., & Lienhard, J. H. V. (1994). Wall roughness effects on stagnation-point heat transfer beneath an impinging liquid jet. *TRANSACTIONS-AMERICAN SOCIETY OF MECHANICAL ENGINEERS JOURNAL OF HEAT TRANSFER*, 116, 81-81.
- Gau, C., & Lee, I. C. (2000). Flow and impingement cooling heat transfer along triangular rib-roughened walls. *International journal of heat and mass transfer*, 43(24), 4405-4418.
- Halbig, M. C., Jaskowiak, M. H., Kiser, J. D., & Zhu, D. (2013, January). Evaluation of ceramic matrix composite technology for aircraft turbine engine applications. In *51st AIAA Aerospace Sciences Meeting including the New Horizons Forum and Aerospace Exposition* (pp. 07-10).

- Han, J. C., Dutta, S., & Ekkad, S. (2012). Gas turbine heat transfer and cooling technology. CRC Press.
- Hansen, L. G., & Webb, B. W. (1993). Air jet impingement heat transfer from modified surfaces. *International journal of heat and mass transfer*, 36(4), 989-997.
- Jeevanlal, V. M., & Kumar, B. A. (2014). Experimental Investigation of Heat Transfer from a Flat and Surface Indented Plate Impinged with Cold Air Jet-Using Circular Nozzle. *International Journal of Emerging Engineering Research and Technology*, 2(5), 160-170.
- Keller, D. A., Schiavo, A. L., & Morrison, J. A. (2011). U.S. Patent No. 7,908,867. Washington, DC: U.S. Patent and Trademark Office.
- Keller, D. A., Gonzalez, M. F., & Morrison, J. A. (2012). U.S. Patent No. 8,202,588. Washington, DC: U.S. Patent and Trademark Office.
- Kito, M., Takezaki, M., Shakouchi, T., Tsujimoto, K., & Ando, T. (2012). Enhancement of Impingement Heat Transfer on a Flat Plate with Ribs. *World Academy of Science, Engineering and Technology*, 6, 1367-1373.
- Koff, B. L., & Koff, B. L. (2004). Gas turbine technology evolution: A designers perspective. *Journal of propulsion and power*, 20(4), 577-595.
- Livingood, J. N., & Hrycak, P. (1973). Impingement heat transfer from turbulent air jets to flat plates: a literature survey.
- Martin, H. (1977). Heat and mass transfer between impinging gas jets and solid surfaces. *Advances in heat transfer*, 13, 1-60.
- Mehta, R. D., & Bradshaw, P. (1979). Design rules for small low speed wind tunnels. *The Aeronautical Journal*, 83(827), 443-453.
- Morrison, J. A., Campbell, C., Merrill, G. B., Lane, J. E., Thompson, D. G., Albrecht, H. A., & Shteyman, Y. P. (2004). U.S. Patent No. 6,709,230. Washington, DC: U.S. Patent and Trademark Office.
- Nakod, P. M., Prabhu, S. V., & Vedula, R. P. (2008). Heat transfer augmentation between impinging circular air jet and flat plate using finned surfaces and vortex generators. *Experimental thermal and fluid science*, 32(5), 1168-1187.
- O'Donovan, T. S., & Murray, D. B. (2006). Effect of vortices on jet impingement Heat Transfer. In *International Heat Transfer Conference 13*. Begel House Inc..
- Ortelt, M., Hald, H., Fischer, I., Greuel, D., Haidn, O., & Suslov, D. (2005, July). Empirical verification of effusion cooled CMC rocket thrust chambers. In

- Proceedings 41st Joint Propulsion Conference (AIAA, Tucson, 2005).
- Renz, R., Seifert, G., & Krenkel, W. (2012). Integration of CMC brake disks in automotive brake systems. *International Journal of Applied Ceramic Technology*, 9(4), 712-724.
- Ricklick, Mark, Phil Poinsatte, Doug Thurman, (2015). Preliminary Assessment of the Implication of CMC Surface Features on Gas Turbine Cooling Methodologies. NASA-Faculty Fellowship Program Final Report, summer 2015.
- Shakouchi, T., & Kito, M. (2012). Heat Transfer Enhancement of Impinging Jet by Notched-Orifice Nozzle (pp. 441-468). INTECH Open Access Publisher.
- Sommers, A., Wang, Q., Han, X., T'Joen, C., Park, Y., & Jacobi, A. (2010). Ceramics and ceramic matrix composites for heat exchangers in advanced thermal systems—A review. *Applied Thermal Engineering*, 30(11), 1277-1291.
- Steibel, J. D., & Utah, D. A. (2001). U.S. Patent No. 6,316,048. Washington, DC: U.S. Patent and Trademark Office.
- Upalkar, B., & Ricklick, M. (2015). Evaluation of different Turbulence Models for analysis of Jet Impingement in Gas Turbine Blades. In 45th AIAA Thermophysics Conference (p. 2812).
- Wagner, C., Kenjereš, S., & von Rohr, P. R. (2011). Dynamic large eddy simulations of momentum and wall heat transfer in forced convection over wavy surfaces. *Journal of Turbulence*, (12), N7.
- Wang, T., & Dhanasekaran, T. S. (2008, January). Calibration of CFD model for mist/steam impinging jets cooling. In *ASME Turbo Expo 2008: Power for Land, Sea, and Air* (pp. 703-716). American Society of Mechanical Engineers.
- Xie, Y., Li, P., Lan, J., & Zhang, D. (2013). Flow and heat transfer characteristics of single jet impinging on dimpled surface. *Journal of Heat Transfer*, 135(5), 052201.
- Xu, P., Sasmito, A. P., Qiu, S., Mujumdar, A. S., Xu, L., & Geng, L. (2016). Heat transfer and entropy generation in air jet impingement on a model rough surface. *International Communications in Heat and Mass Transfer*, 72, 48-56.
- Yan, X., & Saniei, N. (1997). Heat transfer from an obliquely impinging circular, air jet to a flat plate. *International Journal of Heat and Fluid Flow*, 18(6), 591-599.
- Zhong, F., & Brown, G. L. (2009). Experimental study of multi-hole cooling for integrally-woven, ceramic matrix composite walls for gas turbine applications. *International Journal of Heat and Mass Transfer*, 52(3), 971-985.

Zuckerman, N., & Lior, N. (2005). Impingement heat transfer: correlations and numerical modeling. *Journal of heat transfer*, 127(5), 544-552.

